ABSTRACT

Title of thesis: EFFECT OF INTERACTIONAL AERODYNAMICS ON COMPUTATIONAL AERODYNAMICS OF SIKORSKY'S NOTIONAL X2 PLATFORM

Ian Kevin Bahr
Master of Science in Aerospace Engineering, 2020

Thesis directed by: Professor James Baeder
A. James Clark School of Engineering
Department of Aerospace Engineering

An in-house acoustics code, ACUM, was used in conjunction with full vehicle CFD/CSD coupling to create a computational aeroacoustic framework to investigate the effect of aerodynamic interactions on the acoustic prediction of a compound coaxial helicopter. The full vehicle CFD/CSD was accomplished by using a high-fidelity computational fluid dynamics framework, HPCMP CREATE^{TM}-AV Helios, combined with an in-house computational structural dynamics solver to simulate the helicopter in steady forward flight. A notional X2TD helicopter consisting of a coaxial rotor, airframe and pusher propeller was used and split into three simulation cases: isolated coaxial and propeller, airframe and full helicopter configuration to investigate each component's affect on the others noise as well as the total noise. The primary impact on the acoustic prediction was the inclusion of the airframe in the CFD simulation as it affected both coaxial rotors as well as the propeller. It was found that the propeller and coaxial rotors had negligible impact on each other.

EFFECT OF INTERACTIONAL AERODYNAMICS ON COMPUTATIONAL AEROACOUSTICS OF SIKORSKY'S NOTIONAL X2 PLATFORM

by

Ian Kevin Bahr

Thesis submitted to the Faculty of the Graduate School of the
University of Maryland, College Park in partial fulfillment
of the requirements for the degree of
Master of Science
2020

Advisory Committee:
Dr. James Baeder, Chair/Advisor
Dr. Anubhav Datta
Dr. Roberto Celi

Acknowledgments

First and foremost I'd like to thank my advisor, Dr. James Baeder for giving me the amazing opportunity to work on challenging and extremely interesting projects over the past two years. The guidance and advice he provided was irreplaceable during my graduate school experience. I would also like to thank Dr. Anubhav Datta and Dr. Roberto Celi for agreeing to serve on my thesis committee and sparing their invaluable time reviewing my research.

I gratefully acknowledge the help my colleagues and predecessors provided during my research. Bradley Passe and Vera Klimchenko for their preceding work on the X2 platform. Brad Passe paved the way of modeling the coaxial X2TD platform in PRASADUM and coupling this with the Helios framework. Vera deserves special thanks for all her preceding work setting up the grids and simulations for the aerodynamic interactions as well as her help in preparing her aerodynamic results for acoustic analysis. I also thank Dr. J. G. Leishman and coworkers for the availability of the Maryland Free Wake software.

I would like to thank VLRCOE for the funding support for my research as well as the High Performance Computing and CREATE-AV: Helios team for providing the computational resources and technical guidance for this project.

Table of Contents

List of Tables

List of Figures

List of Abbreviations

ABC^{TM}	Advanced Blade Concept
ACUM	Acoustic Code University of Maryland
BDF2	2nd order Backwards Differentiation
BVI	Blade Vortex Interactions
CCW	Counter-Clockwise
CFD	Computational Fluid Dynamics
CG	Center of Gravity
CSD	Computational Structural Dynamics
CW	Clockwise
dB	Decibels
dBA	A-weighted Decibels
DOD	Department of Defense
FFT	Fast Fourier Transform
FVL	Future Vertical Lift
FWH	Ffowcs Williams Hawkings
Hz	Hertz
LOS	Lateral Lift Offset
MFW	Maryland Free Wake
NIHL	Noise Induced Hearing Loss
OASPL	Overall Sound Pressure Level
Pa	Pascals
RMS	Root Mean Square
RPM	Revolutions Per Minute
SA-RANS	Spalart-Allmaras Reynolds-Averaged Navier-Stokes
SPL	Sound Pressure Level
RMS	Root Mean Square
UMD	University of Maryland
VTOL	Vertical Take-off and Landing
VVPM	Viscous Vortex Particle Method
X2TD	X2 Technology Demonstrator

Chapter 1: Introduction

1.1 Motivation

Future Vertical Lift (FVL) vehicles currently have increased interest from both civilian and defense companies. This increased interest can be attributed to the desire to expand the capabilities of vertical take-off and landing (VTOL) aircraft by examining compound configurations outside of the standard main and tail rotor configuration. Compound configurations rely on additional components to augment the lift or thrust of the main rotor seen in typical helicopter configurations. Multiple companies have developed and researched different compound configurations in an attempt to overcome the limitations inherent in the traditional helicopter designs. In 2009, the Secretary of Defense established the FVL Initiative to focus on technology development with the goal to replace all current Department of Defense (DOD) helicopters with next-generation FVL vehicles [1]. The strategy is to examine multiple configurations that are capable of fulfilling myriad roles within the missions for the DOD. One such configuration under review is the compound contra-rotating coaxial helicopter with an auxiliary propeller, specifically the Sikorsky X2 Technology Demonstrator^{TM} (X2TD).

The compound coaxial helicopter overcomes the traditional helicopter forward

Figure 1.1: Sikorsky Advanced Blade Concept (XH-59)

flight limitation by using the Advanced Blade Concept (ABC^{TM}), discussed further in Ref. [2]. The ABC^{TM} (Figure 1.1) maximizes the lift on the advancing side of each rotor disk to offload the lift reduction on the retreating side. Single rotor configurations achieve roll moment equilibrium from the advancing and retreating side of the same rotor disk; however, the ABC^{TM} configuration achieves roll moment equilibrium from the advancing sides of the different rotor disks. Lateral lift offset (LOS) is used to meet the thrust requirements while balancing the roll moment and reducing the blade loads using differential cyclic controls on each disk. Because most of the lift is now carried on the advancing side, the retreating side can be offloaded which will reduce the impacts of retreating blade stall.

The Sikorsky X2 Technology Demonstrator^{TM} expands upon the ABC^{TM} by improving the aerodynamic efficiency of the main rotor at high speeds. This is

Figure 1.2: Sikorsky Advanced Blade Concept

accomplished by incorporating both positive and negative twist gradients as well as a non-uniform planform and modern airfoils [3]. Furthermore, the X2TD incorporates an auxiliary propeller to provide enhanced thrust at higher speeds to counteract the increased drag from the fuselage (Figure 1.2).

All the performance benefits of the X2TD do not come without drawbacks. In order to reduce drag in forward flight, the X2TD main rotor disks must be placed close to one another which forces the blades to have stiffer flap response to maintain the required blade clearance. The proximity of the main rotor disks will also result in interference between the rotors and their wakes. Furthermore, in forward flight the combined wakes from both rotors will interfere with the propeller and the fuselage. Overall, these interactions will produce a complicated flow field with the different aerodynamic bodies all affecting one another. As further research is conducted into more complicated designs to fulfill the FVL initiative, it is important to understand how aerodynamic interactions between different bodies affect the

acoustic predictions.

1.2 Background

A brief background on the sources of noise and how this noise can be measured is provided below. An understanding of the sources of aeroacoustic noise is important to understand the effects of aerodynamic interactions on measured noise discussed in this thesis.

The main sources of noise considered in this thesis were thickness and loading noise.

1.2.1 Thickness Noise

Thickness noise is the noise that results from the pressure fluctuation created by the air displaced from a moving body. Thickness noise is directly related to rotor blade geometry properties such as airfoil shape and geometric twist. Thickness noise is represented as a monopole surface source (discussed in Section 2.3). The thickness noise is generally small compared to loading noise but can equal in magnitude at high tip speeds [4]. The nominal thickness noise distribution can be seen in Figure 1.3a.

1.2.2 Loading Noise

Loading noise is the noise that results from the thrust and torque forces acting along the blade from the pressure distribution along the surface. Loading noise is

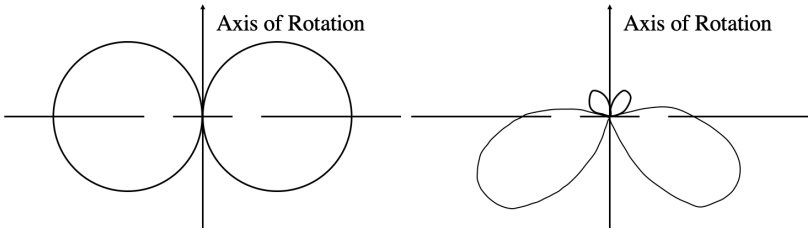

(a) Thickness Noise (b) Loading Noise

Figure 1.3: Polar Plots of Nominal Noise Patterns

represented by a dipole surface source [5] and is directly related to the magnitude of aerodynamic forces and loads along the blade. Loading noise is the dominant contributor to total noise at low to moderate speeds, which is the focus of this thesis. Loading noise is highest out of plane of rotation as seen in Figure 1.3b. The loading noise prediction is contingent upon accurate aerodynamic modeling.

1.2.3 Other Sources of Noise

A major source of noise, outside of the rotor and propeller blades, would be the engines used for the nominal X2TD configuration. At a moderate flight speed of 150 knots the engine noise might not be negligible; however, the focus is on interactional aerodynamic effects on acoustics so this source of noise was not considered.

Another source of noise is broadband noise which exists at a wide range of frequencies. Broadband noise is normally a product of rotor blade interactions with turbulence within the flow around the rotor. This is considered broadband noise because the pressure fluctuations are randomly located in time and space as the rotor blades ingest and cut through turbulent eddies. At low harmonics, this source

of noise can be considered important as the elongation of large turbulent eddies allow them to be cut multiple times resulting in greater pressure fluctuations [6]. However, this source of noise is difficult to predict and not a dominant source of noise for forward flight. Therefore, broadband noise was not included in the analysis of the interactional effects and the total noise experienced by the observers is a summation of thickness and loading noise.

Furthermore, true observers would also be experiencing noise present in their environment and the operating environment of the helicopter. This thesis does not attempt to quantify the total noise that an observer is experiencing but instead how the expected noise of the X2 will change when simulating for the entire configuration versus isolated components.

1.2.4 Measuring Noise

This thesis contains three different measurements for noise experienced by an observer: sound pressure level, overall sound pressure level, and A-weighted decibels.

The sound pressure level (SPL) is defined as the logarithmic ratio of root mean square (RMS) pressure to reference pressure and is commonly expressed in the decibel (dB) scale. This measurement of noise is commonly used across multiple industries and is the method most people are familiar with. The reference pressure (p_{ref}) is defined as the minimum pressure difference heard by humans ($\sim 20\ \mu$Pa) and the RMS pressure (p_{RMS}) is used to quantify the pressure fluctuation from

ambient conditions, as seen in Equation 1.1.

$$dB = 20log_{10}\left(\frac{p_{RMS}}{p_{ref}}\right) \tag{1.1}$$

Figure 1.4 shows the dB values for commons sounds that people normally experience. Normal conversation is approximately 60 dB and noise-induced hearing loss (NIHL) can be caused by noises above 85 dB depending upon exposure time [7].

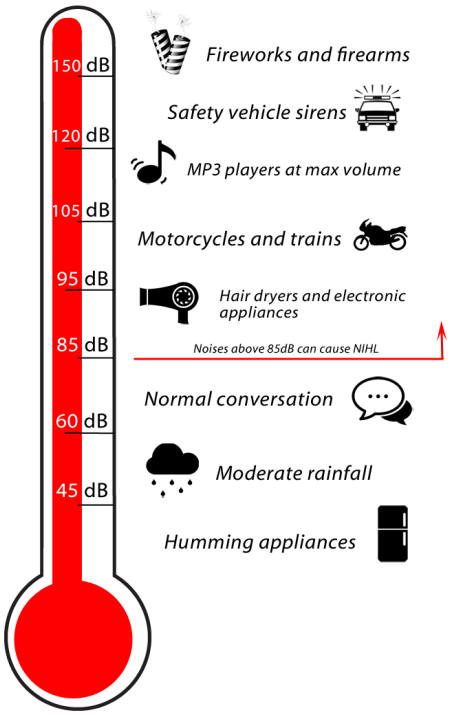

Figure 1.4: Decibel Scale of Common Sounds

The SPL occurs at particular frequencies so overall average sound pressure level (OASPL) is used to show the overall energy contained within the entire spectrum. OASPL takes into account all frequencies that contribute to the pressure-time history from a source. This is calculated using the Fast Fourier Transform (FFT)

discussed in greater detail in Section 2.3. Once the SPL is calculated at each frequency, the summation of those values gives the OASPL. The OASPL is equivalent to the SPL received by integrating across all frequencies.

The final measurement used is A-Weighted Decibels (dBA) which is used to measure the human perception of sound. The measured dB value is corrected to account for relative loudness by weighting frequencies based on the annoyance to the human ear. The detailed calculation and weighting function for OASPL and dBA will be discussed in greater detail in Section 2.3.

1.3 Thesis Contributions

The purpose of this thesis was to investigate the effects modeling aerodynamic interactions have on acoustic predictions. The Sikorsky X2TD was modeled at a moderate forward flight speed of 150 knots in various configurations to evaluate the effect on aeroacoustic predictions. This thesis examines how modeling the fuselage and full helicopter configurations change the acoustic predictions versus modeling the coaxial rotor system and propeller in isolation.

There have also been multiple studies that examine the aerodynamic interactions between coaxial rotors using various models. One such study is conducted by Klimchenko et al ([8] and [9]) and is discussed in greater detail later in this thesis (Chapter 4). Another such study couples Viscous Vortex Particle Method (VVPM) with CFD [10]. Singh and Friedmann approximate loads from a CFD database combined with the VVPM to evaluate performance and wake evolution for

a coaxial rotor system in hover. This study found that the coaxial rotor loads are influenced significantly by the rotor wake which supports the need of examining the wake interactions with the full helicopter components.

Aeroacoustic analysis and prediction of FVL vehicles has become a focal point within the vertical flight community especially with the surge of compound and novel configurations. The sources of noise had been thoroughly studied in the 1990s by NASA Langley [6], but it is necessary to expand this understanding to create better prediction tools for acoustic performance for complex compound configurations.

There has been some previous research into the acoustic prediction of coaxial rotors. In 2006, a study attempted to find acoustic trends by modeling a coaxial rotor and varying certain design parameters. This study was able to conclude that coaxial rotors on average were louder than conventional rotors of equivalent solidity [11].

Another major coaxial rotor noise study was conducted in 2009 at the University of Glasgow [12]. This study used the Vortex Transport Model to analyze a teetering two-bladed coaxial system with varying flap stiffness. The paper concluded that the main noise contribution comes from the retreating upper and advancing lower blade interactions but this noise can be reduced by incorporating greater lift offset. However, this study assumes that the structural flap of the blades can be captured with an equivalent flap spring and rigid blades instead of a more detailed structural dynamics model.

A similar study using CFD/CSD coupling with Helios was conducted by Jia et al [13], which examines the effect of lift offset, flight speed, and rotor-to-rotor

separation distance on the acoustics of the coaxial rotor. This study used the XH-59A rotor blades at flight speeds of 100, 150, and 200 knots. Jia et al found that the magnitude of mid-frequency sound pressure level increases significantly with increasing flight speed and lift offset. While this study does account for the propeller and fuselage in the CSD solver, it does not include their effects in the CFD.

Most recently, there was a study from Penn State University that examined the acoustic predictive capabilities of different fidelity aerodynamic models on a lift-offset coaxial rotor system (XH-59 Figure 1.1). The study used Free Wake, Vortex Particle Method and Computational Fluid Dynamics to calculate the blade loads [14]. This paper focused on the aerodynamic differences between the different solvers and how those aerodynamic differences contribute to varying acoustic predictions. However, this study used an isolated coaxial rotor system without the effects of other bodies within the simulation.

The data from this thesis aims to further the understanding of the acoustic prediction ability of simulation and modeling for FVL configurations. This thesis contributes to the vertical flight community by understanding the impacts of modeling full configuration and aerodynamics on acoustic prediction abilities from complex configurations. Specifically, this thesis will analyze the effects of interactional aerodynamics on the acoustic predictability of the nominal Sikorsky X2TD configuration. Establishing these effects will help gain understanding in the vertical lift community for the acoustic impacts compound configurations as companies seek to expand to new and novel vertical lift designs.

1.4 Outline of Thesis

This thesis focuses on how interactions between different aerodynamic bodies will effect the noise of the overall helicopter. Specifically, it examines how the noise prediction changes when using aerodynamic data from isolated systems (rotors or propeller) and data from a full configuration (helicopter). The rest of the thesis is organized as follows:

- Chapter 2 discusses the methodology used for the aerodynamic and acoustic solvers. It covers in detail the computational fluid dynamics (CFD) solver chosen and simulation details as well as an overview of the coupling with a computational structural dynamics (CSD). The acoustic solver and chosen observer locations are presented. Chapter 2 details the overall computational aeroacoustic framework used for this thesis.

- Chapter 3 discusses the aerodynamic and acoustic results from the models included in the comprehensive analysis tool PRASADUM. These models are low fidelity and are intended to serve as a baseline to examine the affect CFD has on acoustic results.

- Chapter 4 discusses the aerodynamic results from all CFD simulations. The isolated systems are presented first, followed by airframe case and finished with the full helicopter simulation. The aerodynamic results are not the focus of this thesis and are meant to provide a detailed background.

- Chapter 5 discusses the acoustic results from all CFD aerodynamic cases fo-

cused on in this thesis. The specific SPL for each rotor and propeller as well as the OASPL and A-weighted SPL are presented. The difference between aerodynamic configurations is identified and analyzed.

- Chapter 6 summarizes all of the work included in this study and identifies interactional aerodynamic effects on acoustic predictions. This chapter also discusses the recommendations for future analysis.

Chapter 2: Methodology

2.1 Overview of Computational Aeroacoustic Framework

The pressure distribution along both main rotor blades and the propeller blades was calculated using two different CFD solvers: OVERFLOW and FUN3D. This pressure distribution was input into the acoustic solver for the Ffowcs Williams Hawkings (FWH) equation to calculate pressure fluctuations and then output the sound pressure levels. The sound pressure levels were separated into different surfaces of the upper rotor, lower rotor and propeller to understand the contributions from the different surfaces to the overall loudness. This computational aeroacoustic framework is discussed in greater detail below starting with the different CFD solvers used followed by the acoustic solver.

2.2 Aerodynamic Simulations

The overlying aerodynamic framework is CREATE^{TM}-AV Helios which supports OVERFLOW and FUN3D as near-body solvers and a Cartesian background grid for the off-body. All CFD simulations were run using the Spalart-Allmaras Reynolds-Averaged Navier-Stokes (SA-RANS) turbulence model in OVERFLOW

and FUN3D near-body solvers as well as the SAMCART off-body solver. The simulations were run with a time step equivalent to a .25 degree step of the main rotor. In order to examine the interaction effects, the simulations were split into three categories: isolated, airframe, and full configuration. The isolated category examines both the coaxial rotor system and the propeller without the influence of the fuselage and stabilizers. The entire coaxial system was examined together because the upper and lower rotors are analyzed and trimmed together for the comprehensive CSD/CFD coupling (discussed further in Section 2.2.4). The airframe category examines how the presence of the fuselage and stabilizers affect the aerodynamics and thereby the acoustics of the coaxial rotors and propeller independently. Finally, the full configuration category performs a comprehensive analysis of the combined coaxial, airframe, and propeller systems.

2.2.1 Main Rotor Grid and Near-Body Solver

The coaxial rotor blade grids were generated using an in-house algebraic structured grid generator to create the O-O viscous meshes for the notional X2TD blades, shown in Figure 2.1. The surface geometry of the blade grid was discretized into 125 wrap-around points, 129 spanwise points and 55 points in the normal direction which results in .88 million points per blade mesh and 7.1 million points for the coaxial system.

The near-body solver chosen for the main rotor blades was OVERFLOW-D (v2.2n), developed by NASA. The OVERFLOW-D modification to the base OVER-

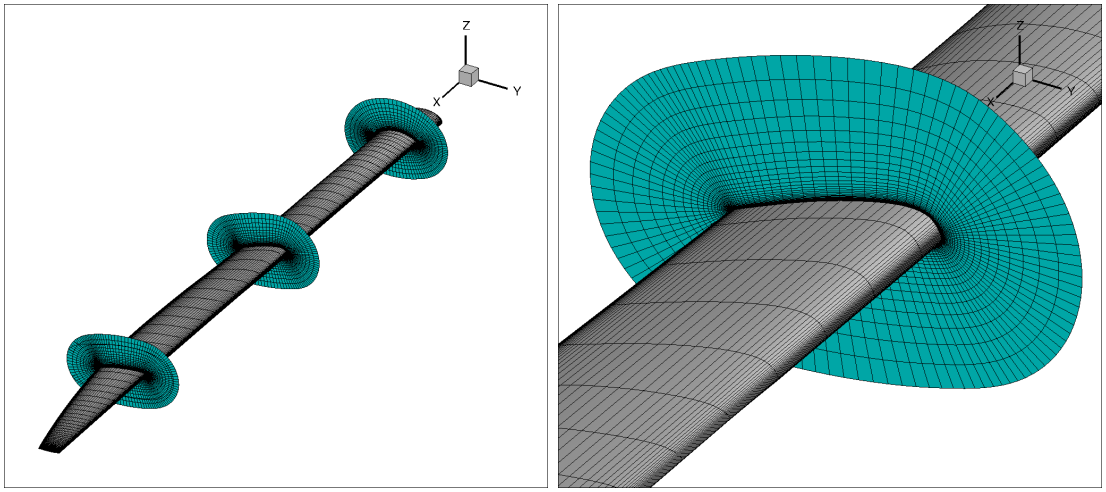

Figure 2.1: O-O Blade Mesh for notional X2 rotor

FLOW code allows for elastic blade motion and grid deformation. This allows for loose CFD/CSD coupling which improves the capture of rotor-rotor, rotor-fuselage, and rotor-propeller interactions [8]. For this research, the simulations were performed using a second-order backward differentiation (BDF2) time-stepping scheme with 20 subiterations with Roe's scheme used for the inviscid fluxes and fourth-order space differencing used to capture the viscous fluxes. The Eddy viscosity was computed using the Spalart-Allmaras turbulence model.

Table 2.1: X2TD Main Rotor Blade Parameters

Parameter	**Value**	
Blade Radius	13.2 ft	4.02336 m
Rotor Tip Speed	620 ft/s	189 m/s
Blade Aspect Ratio	19.2	
Blades per rotor	4	

2.2.2 Fuselage and Propeller Grids and Near-Body Solver

The near-body solver chosen for the fuselage and propeller was FUN3D (v13.3) which is an unstructured NASA CFD solver. The unstructured airframe and propeller grids were generated using CREATE^{TM}-AV Capstone software. The boundary layer is made of prismatic cells and the height of the first layer was chosen so the $y^+ < 1$ at the Reynolds number of $2.6M$ based on the main rotor blade root chord length. There is limited information available on the specific geometry of the X2TD auxiliary propeller so a notional propeller was implemented shown in Table 2.2. The notional propeller has six rigid blades with a linear twist, constant chord, and a constant NACA0012 airfoil.

Table 2.2: Nominal Propeler Blade Parameters

Parameter	**Value**
Number of Blades	6
Blade Radius	3.33 ft 1.015 m
Rotor Tip Speed	882 ft/s 269 m/s
Root Cutout	20 $\%R_{MR}$
Chord	15 $\%R_{MR}$
Twist	-30 deg/span

2.2.3 Off-body solver and Connectivity

The background grid is a Cartesian mesh with seven nested levels of refinement that was generated within the Helios framework. The finest level of refinement was chosen to closely correspond with the cell size of the different near-body grids to promote good interpolation along the boundaries between the near-body and off-

body grids. As seen in Figure 2.2, the finest refinement level is fixed around the blades with a greater emphasis below and behind the blades to ensure that transients in the wake are properly captured.

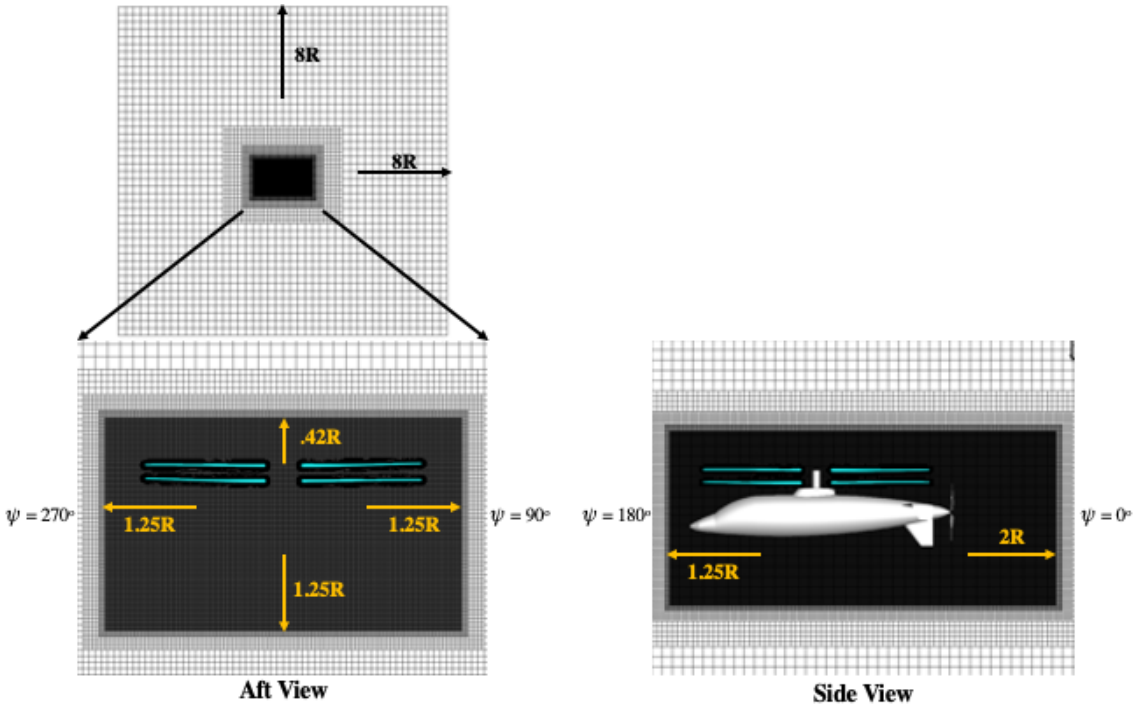

Figure 2.2: Background Cartesian Mesh

Table 2.3: Grid spacing per level for off-body cartesian mesh

Off-Body Refinement Level	Grid Spacing
Level 1	7
Level 2	3.5
Level 3	1.75
Level 4	.875
Level 5	.4375
Level 6	.21875
Level 7	.109375

The coarsest refinement level defines the boundaries of the computational do-

main. The connectivity between the off-body and near-body computational domains is handled by a parallel connectivity module, PUNDIT which is an inherent part of the Helios framework.

2.2.4 CFD/CSD Coupling Methodology

The CSD comprehensive analysis tool used to perform the trim and model the elastic blade deformation of the main rotors was an in-house University of Maryland rotorcraft comprehensive analysis tool, PRASADUM. The main rotor blades were modeled as 1D isotropic Euler-Bernoulli beams undergoing flap, lag, and torsion. Euler-Bernoulli assumes that plane cross-sections of the beam remain planar and the shear deformations can be neglected. A Galerkin based finite element discretization is used to transform the original blade deflection partial differential equations into a system of ordinary differential equations in time. The CSD sectional airloads on the main rotor blades were calculated using 2D airfoil tables, uniform inflow, and unsteady aerodynamics. This use of a simplified lift model was deemed sufficient since these loads are corrected with the high-fidelity CFD airloads [9].

The full vehicle coupling starts with a wind tunnel trim of the propeller to receive the propeller collective for the CFD simulation and match the calculated power with flight test data [15]. Next a full vehicle propulsive trim is performed within PRASADUM to receive the main rotor blade deformations and the vehicle pitch attitude. All of these variables are then included in the CFD simulation and the full configuration is run for two complete main rotor revolutions. The unsteady

main rotor airloads, mean airframe airloads, and propeller yaw moment are extracted from the CFD to correct the values for the next trim iteration. The cumulative delta difference is calculated for the propeller yaw moment and is applied to the CSD yaw moment before re-trimming the propeller to target power [9]. A conventional delta approach is used to calculate the difference between the main rotor CFD airloads and the CSD airloads seen in Equation 2.1.

$$CSD^{i+1} = LO^{i+1} + (CFD^{i} - LO^{i}) = LO^{i+1} + \delta^{i} \tag{2.1}$$

The CSD/CFD coupling was performed by Klimchenko and is discussed in further detail in [8] and [9].

2.2.5 Aerodynamic Post Processing

Once all of the isolated, airframe and full configuration cases were run out to 24 rotor revolutions (12 coupling iterations) for convergence, the near-body surface solutions for the main rotor and propeller were extracted to process the conserved variables. The conserved variables were then used to calculate the pressure coefficient (Equation 2.2) at each node in the wrap-around direction (j) and then along the span (k) at set radial stations.

$$c_{P_{j,k}} = \frac{2.0(p_{jk} - p_{\infty})}{1/2\rho_{\infty}v_{tip}^{2}} = \frac{2\left(\frac{p}{p_{\infty}} - 1\right)}{\gamma M_{tip}^{2}} \tag{2.2}$$

The pressure coefficient was then used to find the normal ($C_N M^2$) and chord ($C_C M^2$) airloads at 40 spanwise locations to properly represent the variation of forces along the blade and the deflection points used for the CSD solver (Equation 2.3).

$$C_{N_k} M^2 = \sum_j \left[\left(\frac{c_{P_{j-1,k}} + c_{P_{j,k}}}{2} \right) \left(\hat{n_j} \cdot \hat{N_k} \right) \right] \frac{M_{tip}^2}{c_k} \tag{2.3}$$

These airloads were calculated at 1440 azimuth locations for the main rotor (every 0.25 degrees) and 254 azimuth locations for the propeller (every 1.42 degrees). The actual time step for all simulations was kept constant, the azimuth step discrepancy is due to the different rotational speeds. A deflection file was then written containing the radial station points used as well as the axial, lag, and flap angles and displacements at each radial station per azimuth (calculated from the CSD). These three files were the required inputs for the acoustics solver.

2.3 Acoustic Solver

The Acoustic Code of the University of Maryland (ACUM) is an in-house acoustic solver that uses compact chord airloads to solve the impermeable surface form of the FWH to obtain the resulting pressure fluctuations. The FWH equation is well known in the aeroacoustic community and requires enclosing the blade near-field information in a computational surface [5].

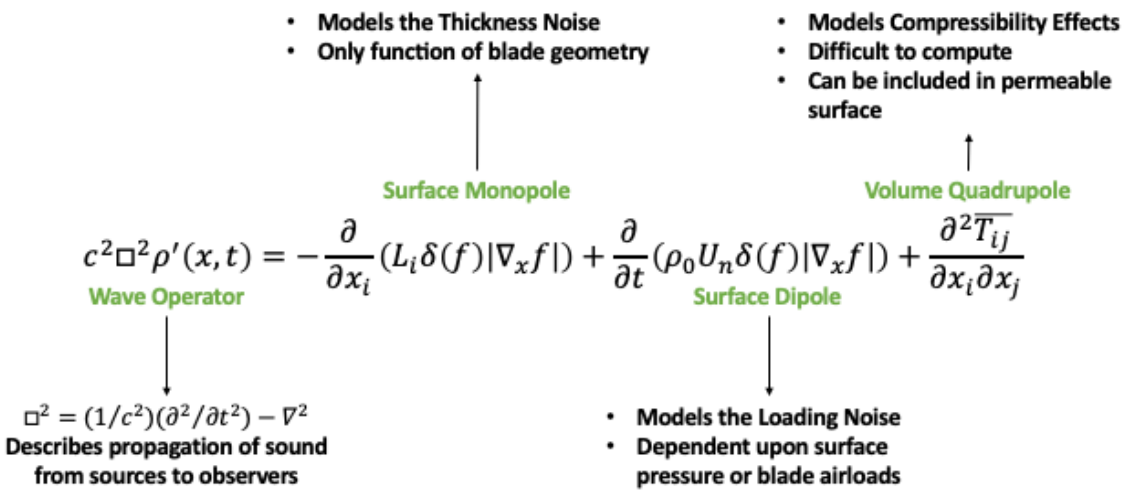

Figure 2.3: Differential Form of Ffowcs Williams and Hawkings Equation

Furthermore, if the computational surface also includes all transonic flow regions then the volume quadrupole term can be neglected. The differential form of the FWH equation and explanation of components is shown in Figure 2.3.

The generation and propagation of sound from a rotor blade is determined by the surface monopole, dipole and volume quadrupole sources (Figure 2.3). The pressure fluctuations calculated from the FWH equation were then converted into SPLs in dB given in Equation 1.1 in Section 1.2.4. Polar observer plots were generated to show the SPL in dB at microphone locations stationed 360^o around the rotor and 6 rotor radii away ($\sim$ 80 ft). The observer locations were chosen to be at varying elevation and azimuthal angles below the rotor because the majority of observers will be concentrated below the helicopter during most flight conditions. Moreover, the hemisphere below the rotor should also contain the highest levels of

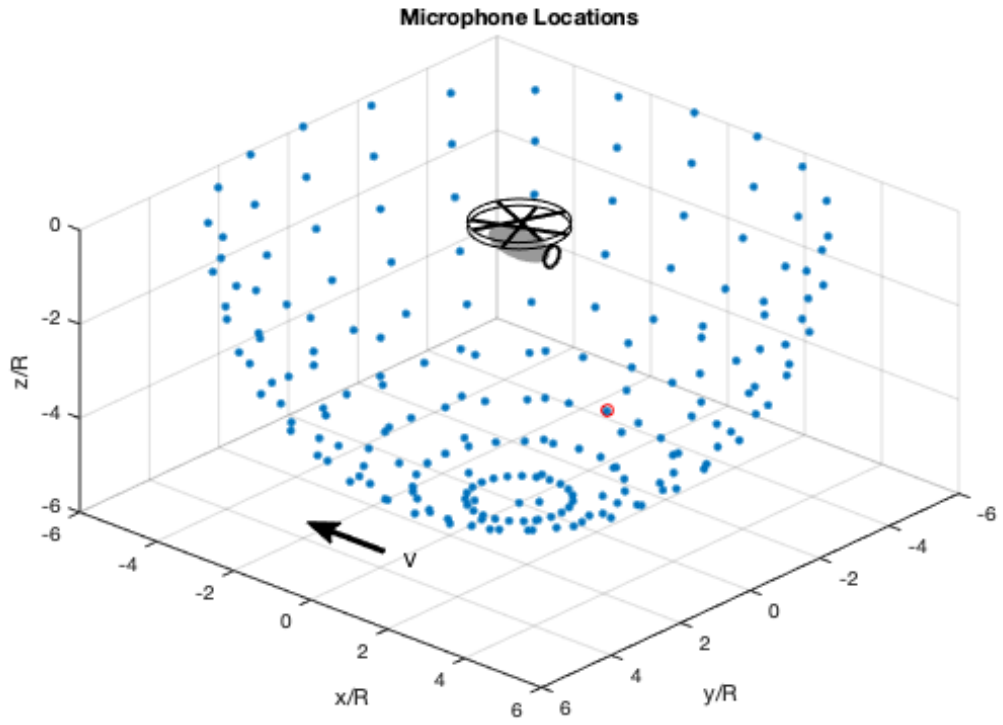

Figure 2.4: Observer Locations in 6R Hemisphere

noise which will provide a greater understanding of the overall helicopter acoustics. The locations were discretized as 15^o in azimuth and 10^o in elevation to form a hemisphere below the rotor as seen in Figure 2.4.

For the full helicopter simulation discussed above (Section 2.2.4), the surface pressure fluctuations are unsteady due to the forward flight speed and presence of fuselage and propeller. Therefore, the expected location of the maximum SPL should change in both azimuth and elevation between the isolated and combined simulations. Therefore, once the SPLs were calculated for all observer locations, the maximum SPL was found for each simulation. As expected, the isolated simulation

had a different maximum SPL location from the airframe and helicopter simulations. For consistency, the overall maximum SPL was chosen to be the full helicopter configuration's maximum SPL at azimuth 90^o (ψ) and elevation 60^o (θ) below the rotor (also shown as a red circle in Figure 2.4). This observer location was used to analyze the pressure-time history in more detail for all of the simulations. The pressure-time history at this location was also used to perform an FFT analysis. As mentioned in Section 1.2.4, the pressure-time history signal at the maximum SPL was broken into multiple frequencies so the SPL at each frequency can be summed into the OASPL.

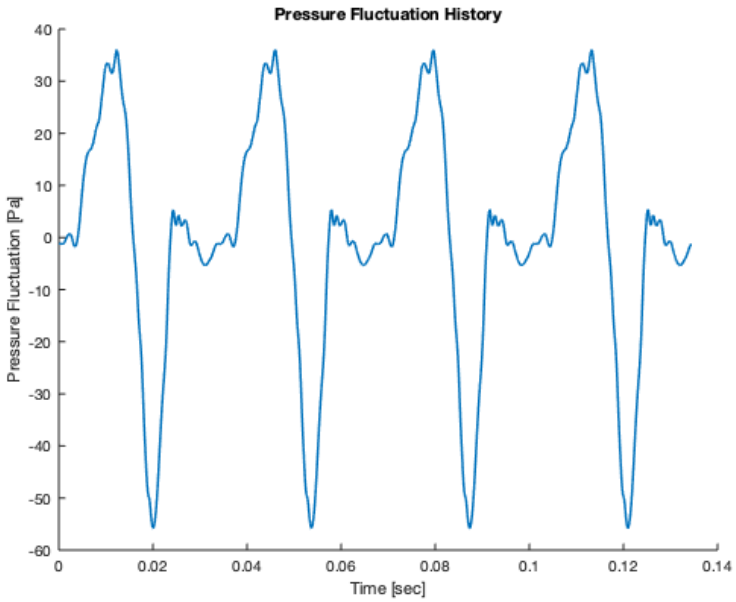

Figure 2.5: Sample Pressure Time History

A sample pressure-time history signal is shown in Figure 2.5. The FFT analysis transforms the time-based pressure signal (measured in Pascals) into the frequency domain. Once in the frequency domain, the pressure signal is changed from Pa to

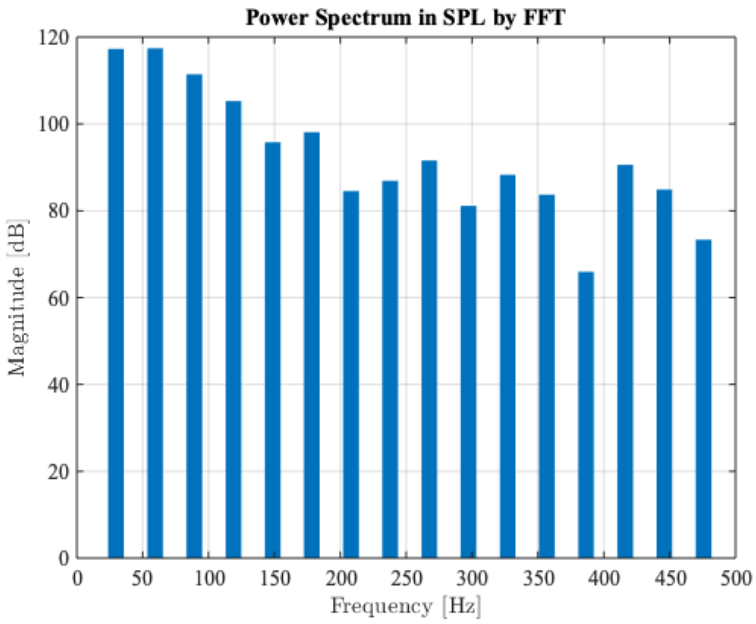

Figure 2.6: Sample Pressure Time History Split Into Frequencies by FFT

dB using Equation 1.1. This gives the final SPL spectrum which shows the dB levels at various frequencies are shown in Figure 2.6. These frequency-based dB levels are then transformed into A-weighted dB (dBA) in the frequency domain.

The A-weighting function is an attempt to correct dB to account for the loudness of different frequencies as heard by the human ear. This is accomplished by applying a dB weighting along the frequency curve shown in Figure 2.7. The A-weighting function is equivalent to 0 dB at 1000 Hertz (Hz) because a human ear is not sensitive one way or the other at this frequency. The dBA scale has a large negative dB weighting for low frequencies to account for the lower sensitivity of human ears. On the other hand, the scale has a slight positive dB weight for frequencies greater than 1k Hz and lower than 6K Hz to account for the greater sensitivity to

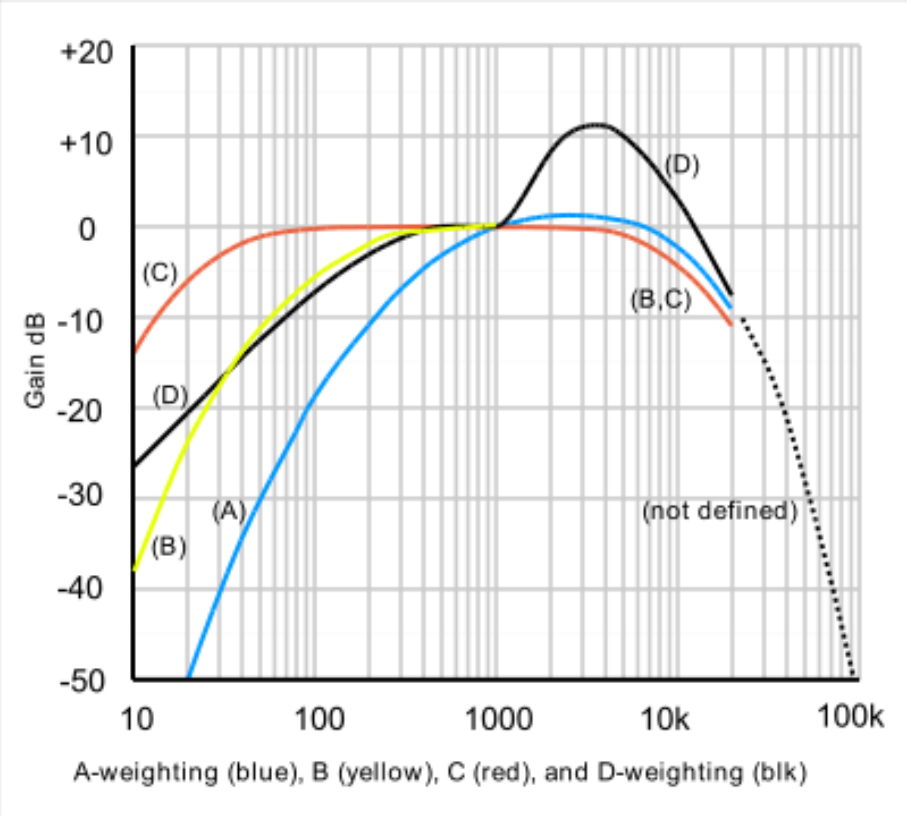

Figure 2.7: A,B,C,D dB Weighting Curves

these frequencies. The A-weighting function, $R_A(f)$ is shown in Equation 2.4 and the actual A weight applied to the dB level is calculated in Equation 2.5.

$$R_A(f) = \frac{12194^2 f^2}{(f^2 + 20.6^2)\sqrt{(f^2 + 107.7^2)(f^2 + 737.9^2)}(f^2 + 12194^2)} \tag{2.4}$$

$$AWeight = 20log_{10}\left(R_A(f)\right) + 2.00 \tag{2.5}$$

The dB value at each frequency is then added with the A weight above to calculate the dBA:

$$dBA = dB + AWeight \tag{2.6}$$

After all dB and dBA values are found at all frequencies, they are summed to calculate the OASPL in both dB and dBA:

$$OASPL(dB) = 10log_{10} \sum 10^{dB/10} \tag{2.7}$$

$$OASPL(dBA) = 10log_{10} \sum 10^{dBA/10} \tag{2.8}$$

The OASPL in dB and dBA is used to compare the overall loudness of the different simulation configurations. In order to have a greater understanding of the interactional effects, it is more beneficial to examine the noise at each observer location in both dB and dBA for each of the configurations. Therefore, a greater amount of analysis is focused on the observer hemispheres and examining any differences or trends that can be found.

Chapter 3: Comprehensive Analysis Results

The coaxial rotor system airloads and acoustics were first calculated using the aerodynamic solvers within the comprehensive analysis tool PRASADUM to have a greater understanding of the impact of CFD/CSD coupling on aerodynamics and acoustics. The aerodynamics for the coaxial rotor trim were calculated within PRASADUM using uniform inflow and free wake at various azimuthal resolutions ($\Delta\psi$) of 10, 5 and 2.5 degrees. The uniform inflow is calculated as a function of the trim process but the free wake is a separate module within the comprehensive analysis and functions as a loose coupling with the CSD portion of PRASADUM. The free wake module within PRASADUM is based on the Maryland Free Wake (MFW) developed by Bhagat and Leishman and is discussed in more detail in Ref. [16]. The time-accurate solver remains unchanged but the input and output formats were optimized for PRASADUM integration. These simulations account for the fuselage and propeller within the CSD trim but do not include any aerodynamic contribution from the fuselage or propeller. This chapter will go investigate the aerodynamic and acoustic results from the comprehensive analysis tool PRASADUM.

3.1 Uniform Inflow

The uniform inflow simulations were calculated exclusively within PRASADUM without any coupling. These simulations only include the coaxial rotor system and are equivalent to the propulsive trim portion of the CFD/CSD coupling methodology (Section 2.2.4). This low fidelity model was used to trim the coaxial rotor system using the same inputs as the CFD/CSD coupling except the delta airloads were neglected.

3.1.1 Upper Rotor with Uniform Inflow

This section will focus on the aerodynamic and acoustic results of the upper rotor simulated with uniform inflow. Figure 3.1 shows the variations in airloads and noise between the different azimuthal resolutions. The normal and chordwise force distributions are smooth across the entire disk as anticipated from uniform inflow. The advancing side of the disk displays a normal force tip loss characteristic of the simple inflow model. The retreating side displays a loss in normal force along the root portion of the blade due to retreating blade stall. These effects should be lessened compared to a typical configuration due to the lift offset mechanism within PRASADUM. Similarly, the chordwise force presents the optimal distribution as expected for a uniform inflow model.

Overall, there is little noticeable difference between the different azimuthal resolutions. Each simulation displays smooth spanwise and azimuth-wise airloads. Table 3.1 shows the control angles for both rotors in the simulations which show

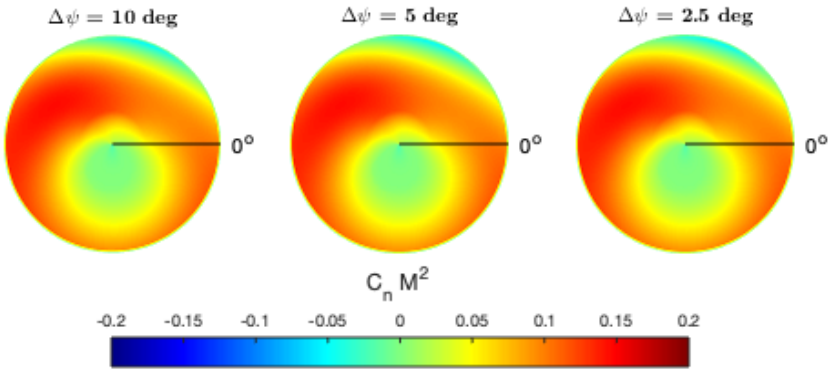

(a) Normal Force

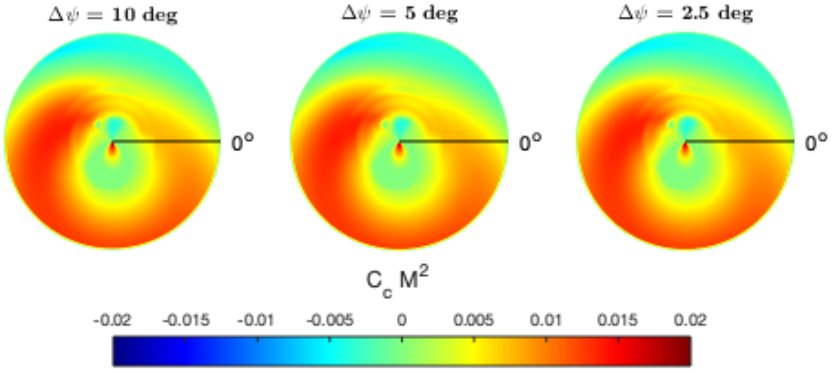

(b) Chordwise Force

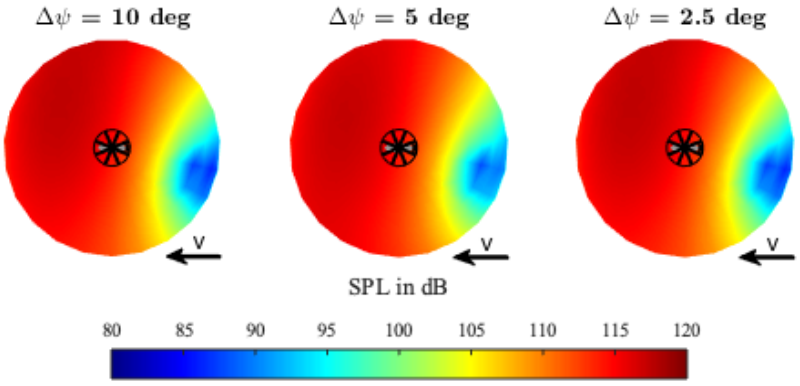

(c) SPL Hemisphere in dB

Figure 3.1: Upper Rotor Aerodynamics and SPL from Uniform Inflow

little change between the different azimuthal resolutions. These small, practically negligible, angle fluctuations predictably lead to little change in airloads and therefore little change in the predicted noise as seen in Figure 3.1c.

Table 3.1: Control Angles from Uniform Inflow for Varying Azimuthal Resolutions

	$\Delta\psi$=**10 deg**	$\Delta\psi$=**5 deg**	$\Delta\psi$=**2.5 deg**
Collective (deg)	5.35 (CCW) 5.33 (CW)	5.35 (CCW) 5.33 (CW)	5.34 (CCW) 5.34 (CW)
Cyclic θ_{1C} (deg)	-0.28 (CCW) -0.28 (CW)	-0.28 (CCW) -0.28 (CW)	-0.28 (CCW) -0.28 (CW)
Cyclic θ_{1S} (deg)	-3.69 (CCW) 3.67 (CW)	-3.70 (CCW) 3.67 (CW)	-3.71 (CCW) 3.68 (CW)

The SPL contours shown in Figure 3.1c display a large amount of noise considering the smooth airloads. The smooth airloads would signify this model calculates less pressure fluctuations both spanwise and azimuth-wise across the rotor disk. In order to understand the cause of the high noise, the pressure-time history can be examined along with the FFT analysis of the signal. The pressure azimuth his-

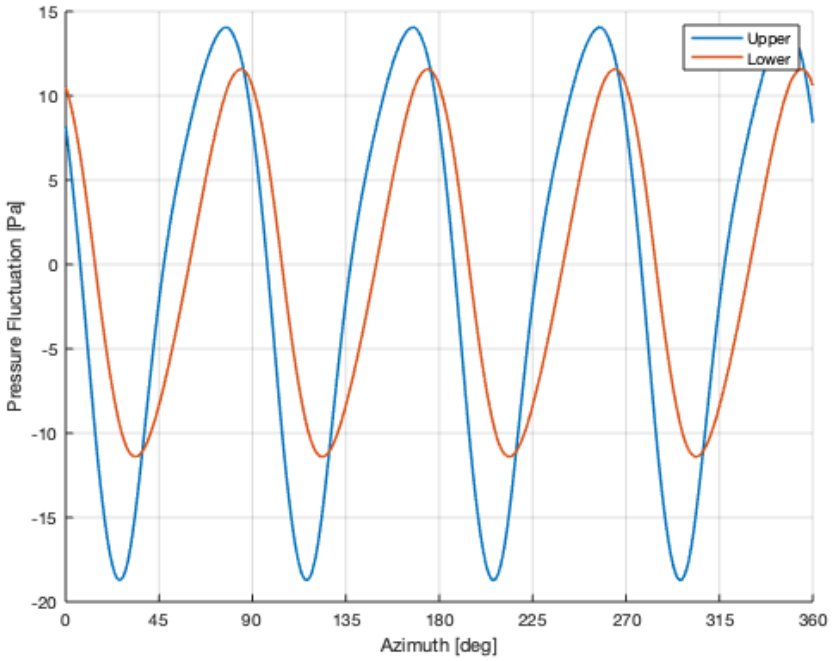

Figure 3.2: Azimuth Pressure History

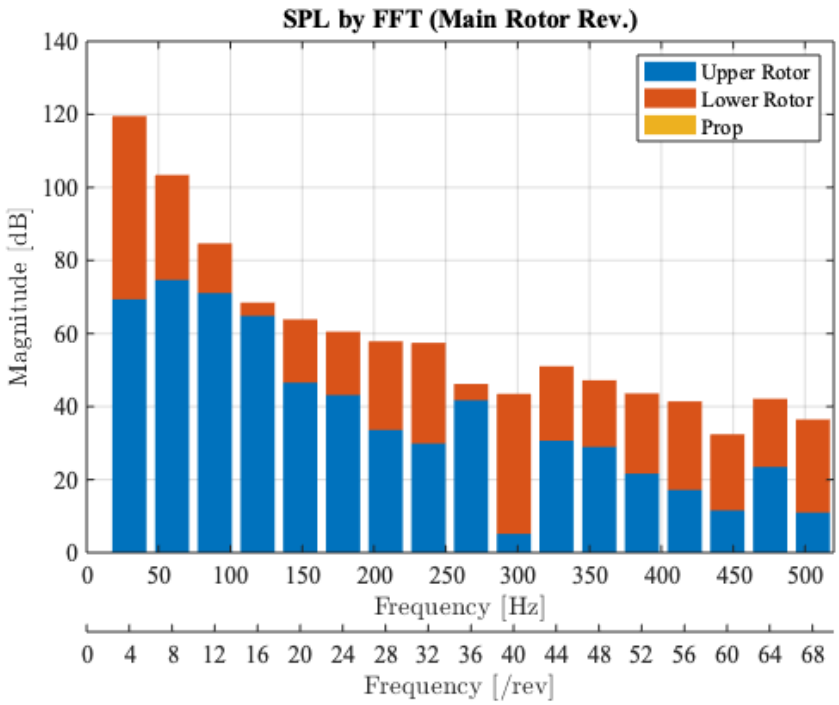

Figure 3.3: SPL of Coaxial Rotors by Frequency for Uniform Inflow

tory in Figure 3.2 is completely smooth for both rotors with seemingly zero high frequency content with a greater contribution from the upper rotor. This difference in contribution is due to the location of the pressure signal and will differ across the observer hemisphere. The FFT analysis in Figure 3.3 confirms that the SPL from uniform inflow is dominated by the low frequency main rotor harmonics of 4/rev and 8/rev signals.

3.1.2 Lower Rotor with Uniform Inflow

This section will focus on the aerodynamic and acoustic results of the lower rotor simulated with uniform inflow. Figure 3.4 shows the variations in airloads and

noise between the different azimuthal resolutions. From the pressure azimuth history and FFT analysis conducted above, it is expected that the lower rotor airloads and SPL will mirror those on the upper rotor. This is indeed the case as the lower rotor

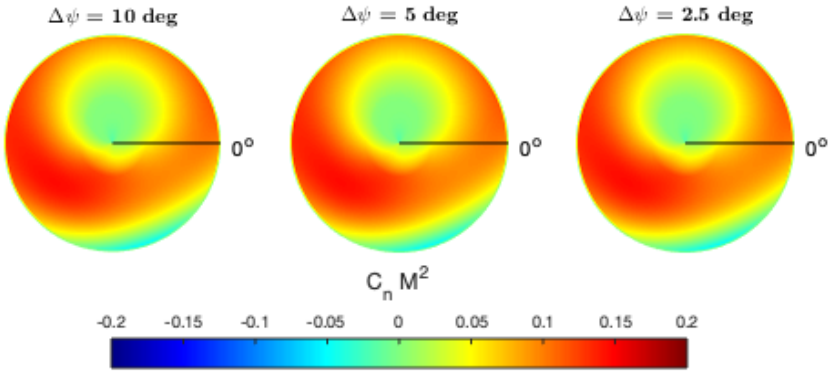

(a) Normal Force

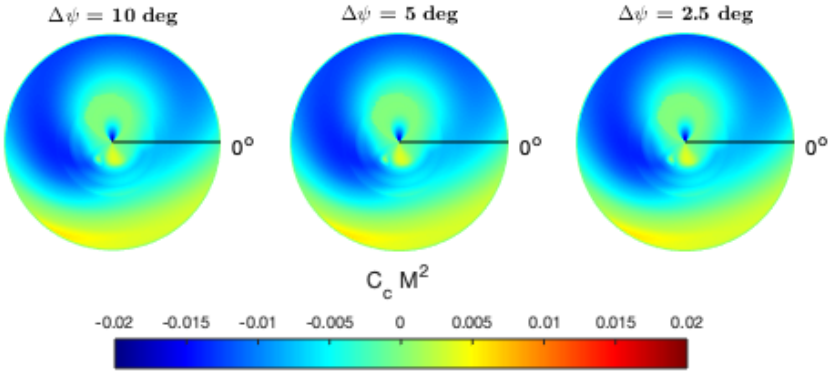

(b) Chordwise Force

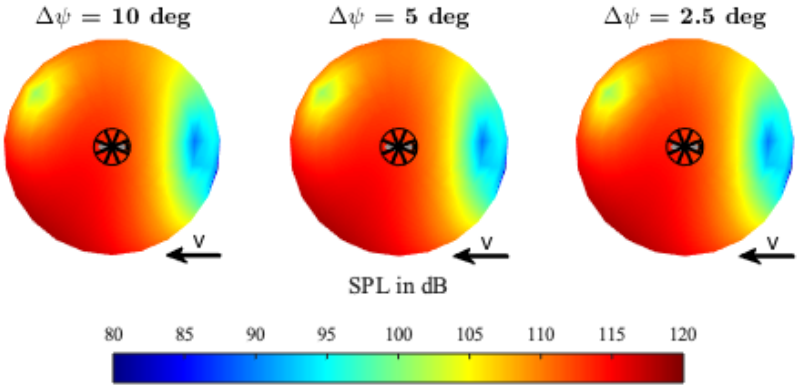

(c) SPL Hemisphere in dB

Figure 3.4: Lower Rotor Aerodynamics and SPL from Uniform Inflow

normal force shows little variation between the different azimuth resolutions and is similar in distribution and magnitude to the upper rotor. The only difference is the lower rotor rotates clockwise meaning that the advancing side is now on the bottom of the contour. The chordwise force on the other hand is weaker in magnitude towards the end of the retreating side of the rotor disk (ψ=315). This decrease in chordwise force should cause a weaker thickness noise which is indeed evident in Figure 3.4c. The SPL contour of the lower rotor has a low region ahead of the rotor as well as a greater low noise region behind the rotor.

Overall, there is little noticeable difference between the different azimuthal resolutions for both the upper and lower rotors. This is further supported by Table 3.1 which shows the control angles for both rotors in the simulations. The control angles show little fluctuation between the different azimuthal resolutions which would indicate for this low fidelity model, the 10-degree resolution is enough. The pressure-time history and FFT analysis demonstrate that the simple uniform inflow model can not capture any high-frequency content. The frequencies with large acoustic content are the main rotor frequencies of 4/rev and 8/rev.

3.2 Free Wake

The free wake simulations were calculated within PRASADUM with a varying wake discretization of 10, 5, and 2.5 degrees. The simulations held the wake turns and bound vortex segments constant between simulations at 6 and 40 respectively. The free wake solver is a part of the PRASADUM framework but is treated as

a coupling solver similar to the CFD/CSD coupling. For these simulations, the free wake solver replaces the CFD in the coupling algorithm. This provides a closer simulation framework to the CFD/CSD coupling for the coaxial rotor system except with a lower fidelity aerodynamic solver. The results for the individual coaxial rotors is discussed in detail below.

3.2.1 Upper Rotor with Free Wake

The free wake solution for the upper rotor shows a greater deviation in results between the different azimuthal resolutions compared to the uniform inflow model. The normal force has a similar profile compared to the linear inflow on the retreating side of the blade but shows an increase in the reverse flow region as azimuthal resolution increases. The more important difference is the presence of higher frequency content along the advancing side as evidenced by the azimuthal and spanwise fluctuations in Figure 3.5a. These fluctuations become sharper as the azimuth resolution increases and could be a result of the free wake capturing the interactions of the upper and lower rotor blade passage.

The chordwise force in Figure 3.5b also demonstrates fluctuations on the advancing side as well as an increase along the entire rotor disk. These pressure fluctuations and increase in airloads has a noticeable effect on the SPL hemispheres in Figure 3.5c. Nearly all observers experience 115 dB of noise with some hearing a maximum of 120 dB. The number of observers that experience of the maximum noise increases as the resolution increases.

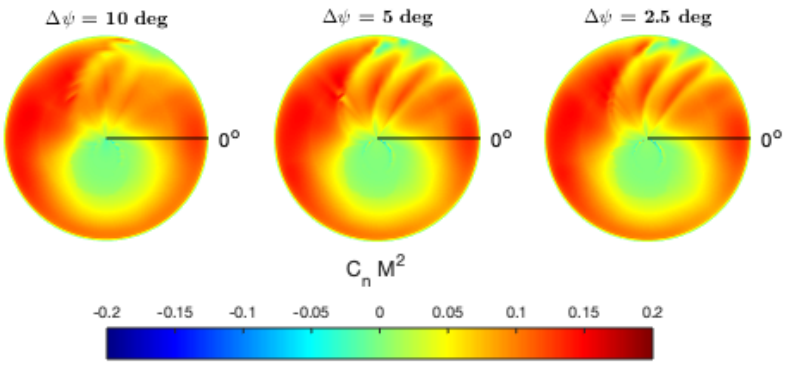

(a) Normal Force

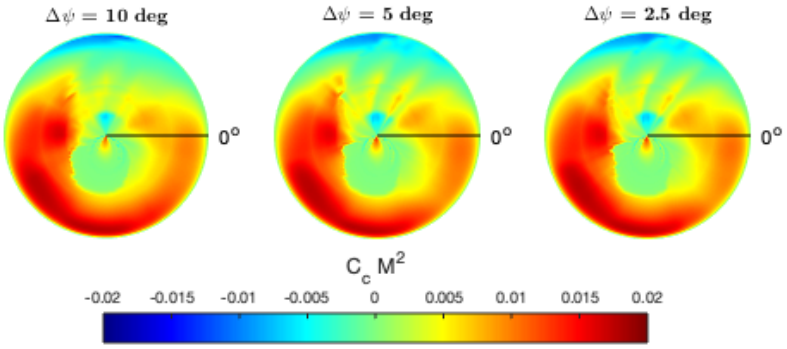

(b) Chordwise Force

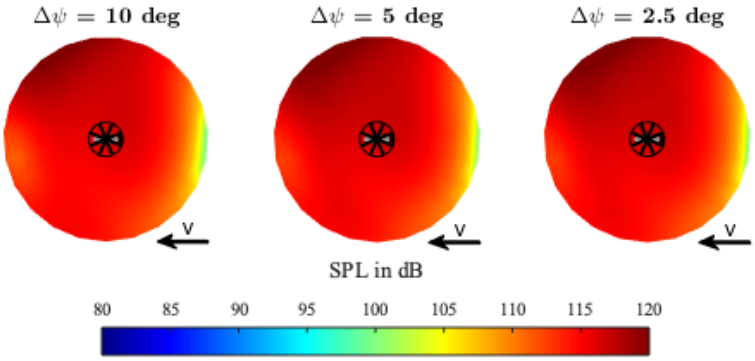

(c) SPL Hemisphere in dB

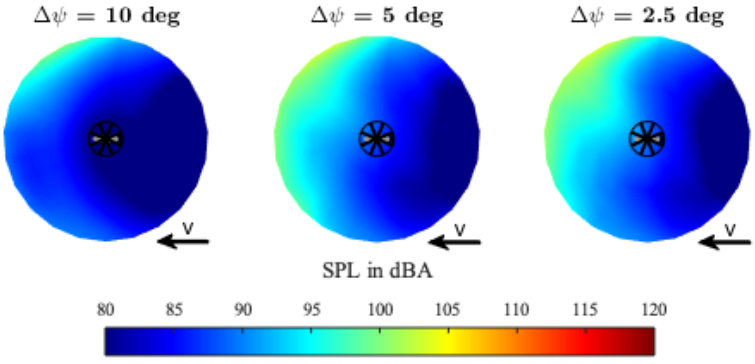

(d) SPL Hemisphere in dBA

Figure 3.5: Upper Rotor Aerodynamics and SPL from Free Wake

While the dB SPL contours show similar trends, the A-weighted dB contours (Figure 3.5d) are similar for the $\Delta\psi$=5 and 2.5 degree cases but vastly different for the $\Delta\psi$=10 degree case. This would indicate that the 10 degree case does not capture the higher frequency content compared to the 5 and 2.5 degree cases. Comparing the pressure time histories and FFT analyses of the $\Delta\psi$=10 and 2.5 will demonstrate the captured frequencies with greater clarity. Figure 3.6 shows that the upper rotor noise is a strong 4/rev signal for the 10 degree case but the 2.5 degree case not only has a greater magnitude but also posses higher frequency content. The presence of these higher frequencies would decrease the A-weighting and explain the increase in dBA noise. This is also evidence that the free wake model is capable of capturing some interaction effects from the lower rotor onto the upper rotor.

3.2.2 Lower Rotor with Free Wake

The more noticeable change in Figures 3.6 and 3.7 are in the lower rotor signal. The 10 degree resolution provides some evidence of high-frequency content but the 2.5 degree resolution calculates the lower rotor contributing more noise across almost all frequencies. The FFT analysis for the $\Delta\psi = 2.5$ degree case shows that the lower rotor dominates all frequencies higher than 12/rev. This provides further evidence that the free wake model is capable of capturing some interaction effects on the lower rotor from the upper rotor.

The normal force distribution on the lower rotor has a slightly larger magnitude compared to the upper rotor. This is most noticeable along the outboard section of

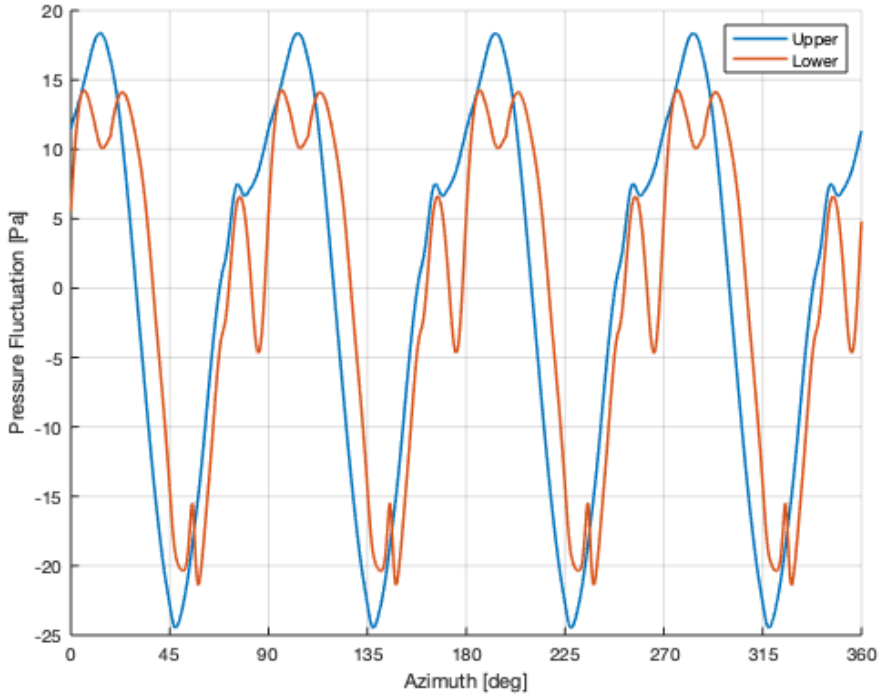

(a) $\Delta\psi$=10 deg

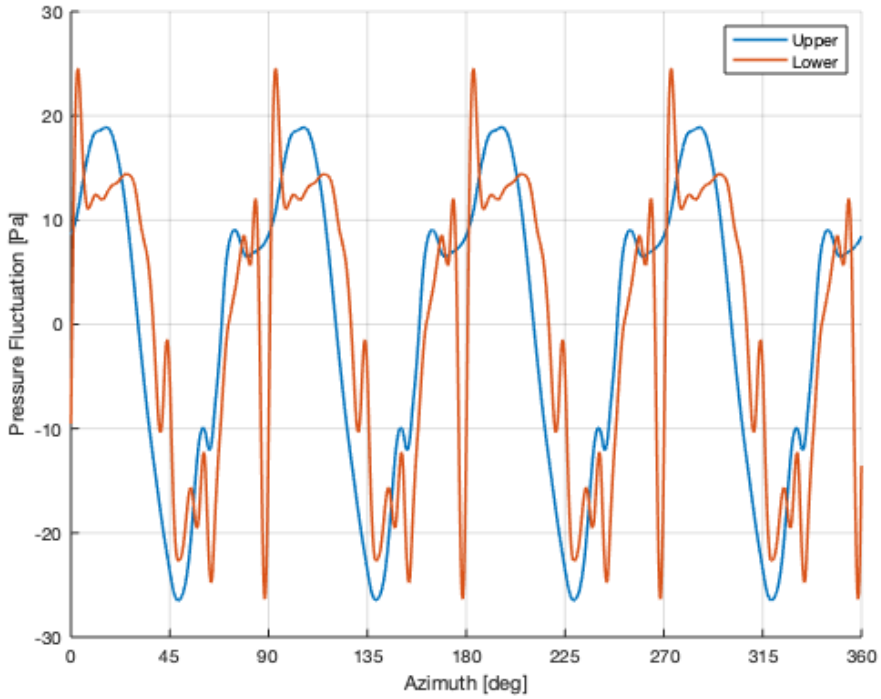

(b) $\Delta\psi$=2.5 deg

Figure 3.6: Azimuth Pressure History for Free Wake

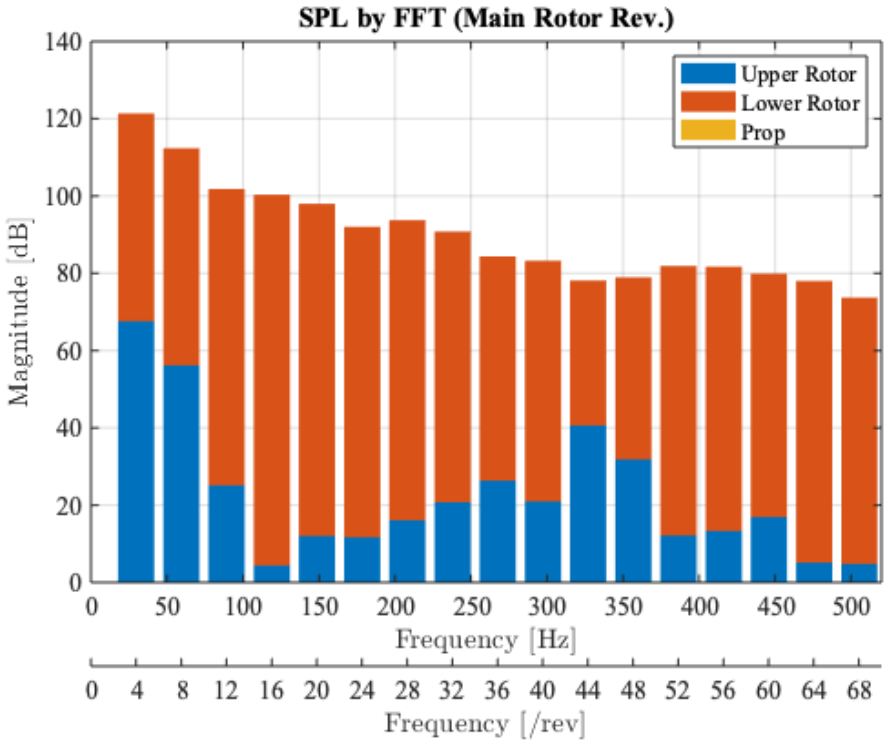

(a) $\Delta\psi$=10 deg

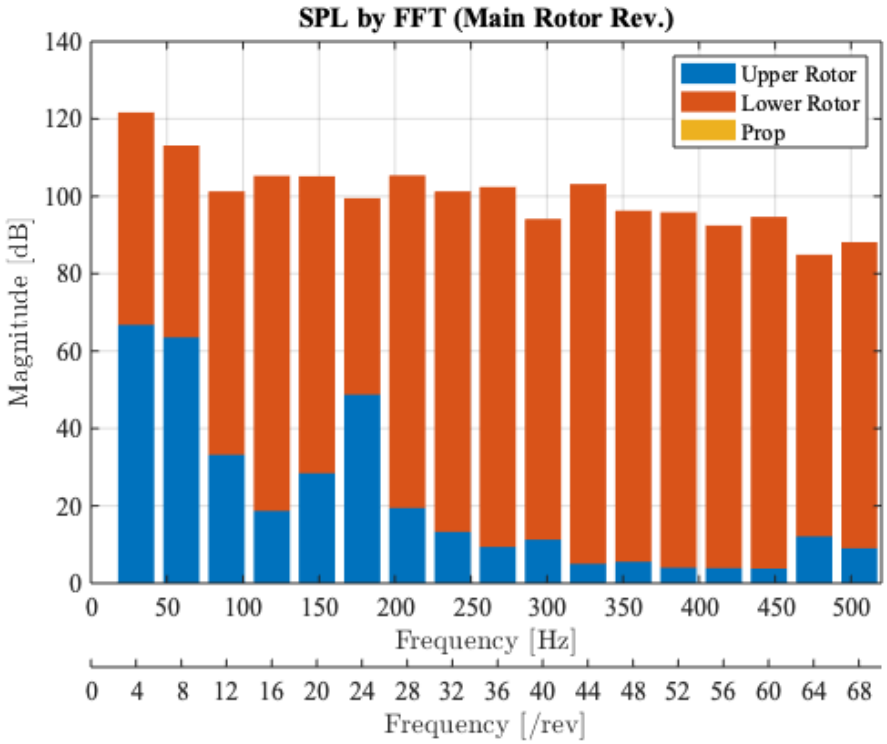

(b) $\Delta\psi$=2.5 deg

Figure 3.7: SPL of Coaxial Rotors by Frequency for Free Wake

the blades on the advancing and retreating side. The blade crossing fluctuations in Figure 3.8a are more pronounced on the lower rotor than the upper rotor. The fluctuations also exhibit a higher normal force peak at the finer resolutions which coincides with the magnitude increase seen in the pressure azimuth signal.

The chordwise force in Figure 3.8b also demonstrates the advancing side blade crossings. Furthermore, the chordwise force is much stronger on the retreating side of the lower rotor than the upper rotor with a large area maximum magnitude. Despite the larger airloads along the lower rotor disk, the dB SPL in Figure 3.8c is quieter than the upper rotor SPL. The SPL increases as the azimuth resolution gets finer which matches the trend seen in the upper rotor.

The most drastic difference from the upper rotor is the A-weighted SPL contours as expected based on the FFT analysis and pressure signal. The maximum dBA noise occurs for the $\Delta\psi =$. 5 degree case which does not match the trends observed for the dB for either rotor. This is unexpected as any high-frequency content should become more refined as the resolution increases. This could indicate that the 5 degree case is calculating frequency content that the 2.5 degree case is then filtering out.

The increase in aerodynamic forces on the both rotors has a noticeable impact on the predicted acoustics. Both rotors exhibit an increase in SPL from free wake across the entire hemisphere compared to the uniform inflow model. The increase is partially caused by a similar increase in rotor airloads on both the upper and lower rotors. The other cause is the capturing of the blade crossing interactions within the free wake model which causes pressure fluctuations along the blades.

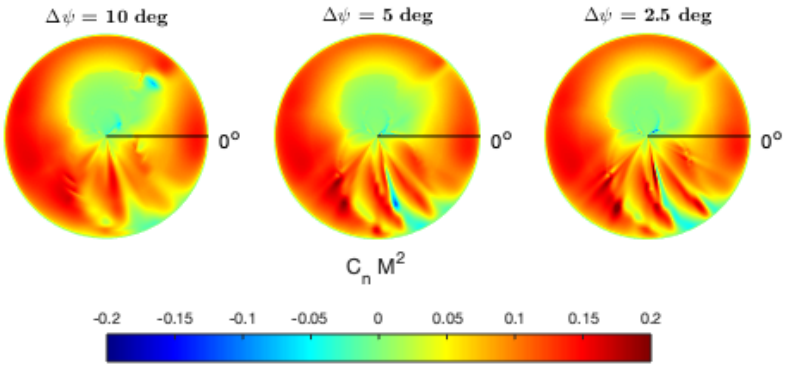

(a) Normal Force

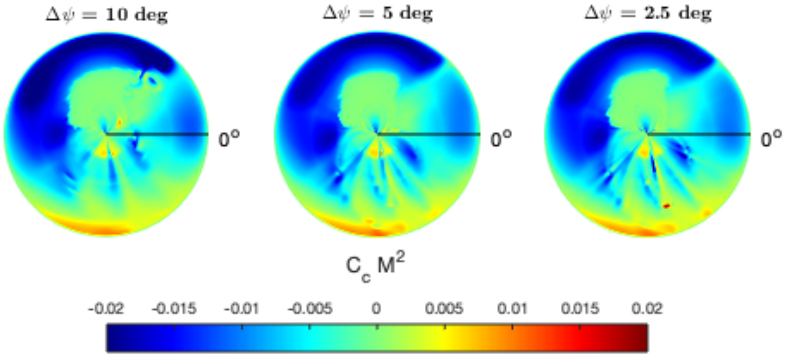

(b) Chordwise Force

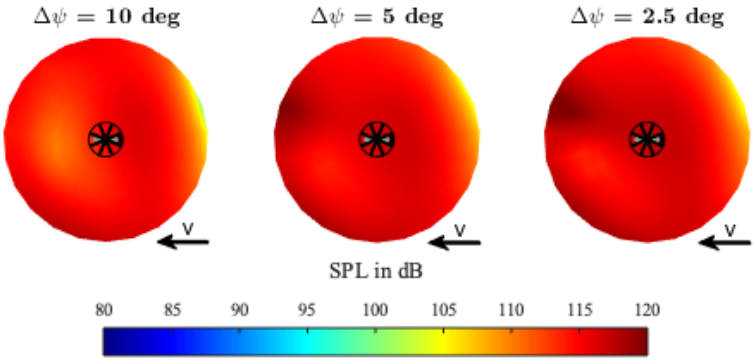

(c) SPL Hemisphere in dB

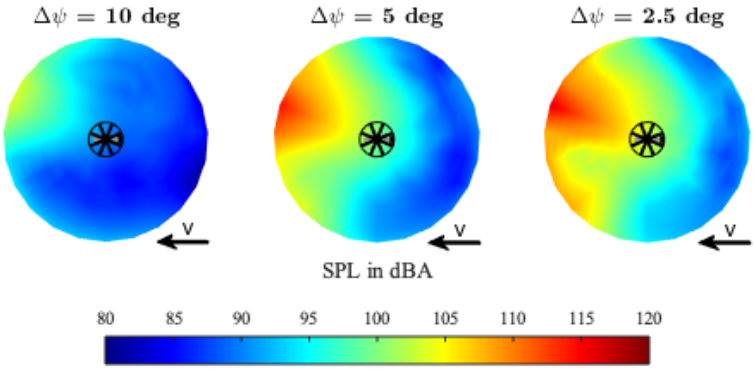

(d) SPL Hemisphere in dBA

Figure 3.8: Lower Rotor Aerodynamics and SPL from Free Wake

Overall, the free wake model demonstrates improvements over the uniform inflow model by capturing the airloads and acoustics in greater detail. The free wake model demonstrates the ability to capture some higher frequency content, most notable the blade crossing interactions between rotors. However, due to the proximity of the rotors and the flight speed it is expected to see a greater unsteadiness in the airloads and therefore acoutsics from BVI and rotor-wake interactions. The free wake model within PRASADUM does not seem capable of capturing these effects; therefore, it is necessary to use a higher fidelity model to solve for the aerodynamics in order to accurately capture the effect aerodynamic interactions have on acoustics.

Chapter 4: Aerodynamic Results

The following sections will describe the aerodynamic results done in preceding work by Klimchenko et al. ([8],[9]). The acoustic results discussed in detail in this thesis are derived from the aerodynamic work in these papers. The focus of this thesis is on the full helicopter acoustic analysis for the 150-knot forward flight speed case so the primary reference is Klimchenko and Baeder [9]. The grid system and CFD/CSD coupling used in these references are the same used for the following acoustic results and are discussed in further detail in Chapter 2. The specific case parameters for the 150-knot forward flight speed results are shown in Table 4.1.

Table 4.1: CFD Interactional Aerodynamics Case

V_∞**(knots)**	μ	**MR RPM**	$\mathbf{M_{adv.\ tip}}$	**LOS(%)**	**Blade Modes**	**Harmonics**
150	0.41	446	0.79	11.3	6	8

4.1 Full Helicopter CFD/CSD Coupling

This section summarizes the effects of the full CFD/CSD coupling on control angles for the coaxial rotors and airframe attitude. Nine coupling iterations were performed for the full configuration CFD/CSD case to ensure that the trim

parameters did not vary significantly with consecutive iterations. For the vehicle to be in trim, the force and moment equilibrium must be enforced at the center of gravity (CG) for each rotor revolution. The force and moment contributions from the various components are closely tied to the control angles and airframe attitude. Moreover, the force contributions from the rotors and propeller will affect the acoustics. Therefore, this section will focus on the changing main rotor controls and the subsequent effect on the forces and moments. The changes in control angles and pitch attitude is summarized in Table 4.2.

Table 4.2: Control Angles for Coaxial and Full Configuration Coupling at 150 knots

	Coaxial CFD/CSD	**Full Vehicle CFD/CSD**
Collective (deg)	6.02 (CCW) 5.95 (CW)	5.76 (CCW) 7.04 (CW)
Cyclic θ_{1C} (deg)	0.96 (CCW) 0.96 (CW)	2.43 (CCW) 2.43 (CW)
Cyclic θ_{1S} (deg)	-5.49 (CCW) 5.16 (CW)	-5.63 (CCW) 6.54 (CW)
Fuselage Pitch (deg)	2.01	2.85

The collective angles for the upper and lower rotor trimmed to relatively similar values in the isolated coaxial system. However, when the airframe and propeller were included the upper rotor collective was reduced while the lower rotor collective increased. The collective difference is caused by the change in the airframe yaw moment. In the isolated coaxial case, the CSD solver assumes the airframe roll and yaw moments are zero at the CG and calculates a nose-down pitching moment due to the horizontal stabilizers. In the full configuration case, the roll, pitch, and yaw moments are non-zero due to CFD calculating loads on the airframe. Namely, the

airframe produces a clockwise yaw moment requiring the coaxial rotors to introduce a yaw moment to oppose the airframe. Therefore, the upper rotor collective is reduced and the lower rotor collective is increased to provide a counter-clockwise moment that balances the airframe yaw moment [9].

Similarly, the cyclic angles θ_{1C} and θ_{1S} increase from the isolated case to the full configuration case. The nose-down pitching moment of the fuselage decreases drastically from the CSD prediction to the full vehicle CFD [9]. Therefore, the increase in θ_{1C} control angle subsequently reduces the pitching moment of the rotors so that the airframe and rotors stay in equilibrium. The full vehicle CFD/CSD produces a port side down roll moment at the CG from the airframe. In response, the magnitude θ_{1S} is increased for both rotors with the lower rotor θ_{1S} trimmed to a higher value. This produces a starboard side down roll moment to counteract the airframe roll moment.

The full vehicle CFD/CSD also demonstrates an increase in propeller thrust compared to the isolated case. For the coaxial CFD/CSD coupling, the propeller thrust is approximated using $P = TV$, where P is propeller power for the X2TD given in Ref. [17]. Conversely, the full vehicle CFD/CSD the propeller thrust is obtained from the actual CFD airloads for the propeller trimmed to the given power in Ref. [17].

4.2 Interactional Aerodynamics Affecting the Upper Rotor

This section will focus on the aerodynamic interactions affecting the upper rotor that arise when analyzing the coaxial rotor in isolation as well as in conjunction with the airframe and full vehicle.

Figure 4.1a shows the non-dimensional azimuthal normal force distribution for the various configurations (ψ=0 on right side). For the coaxial rotor system in

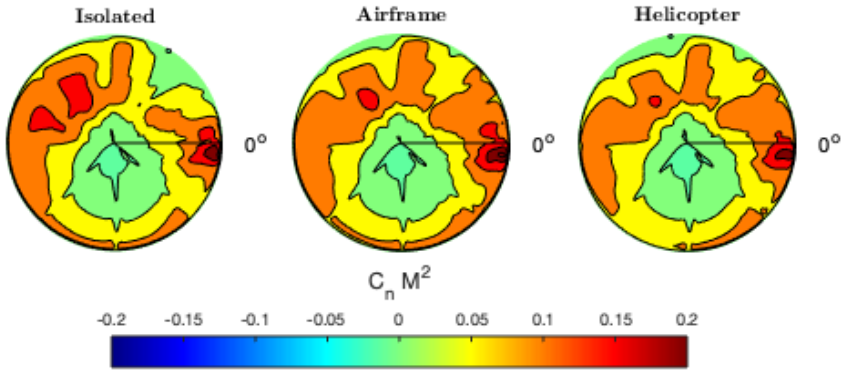

(a) Normal Force

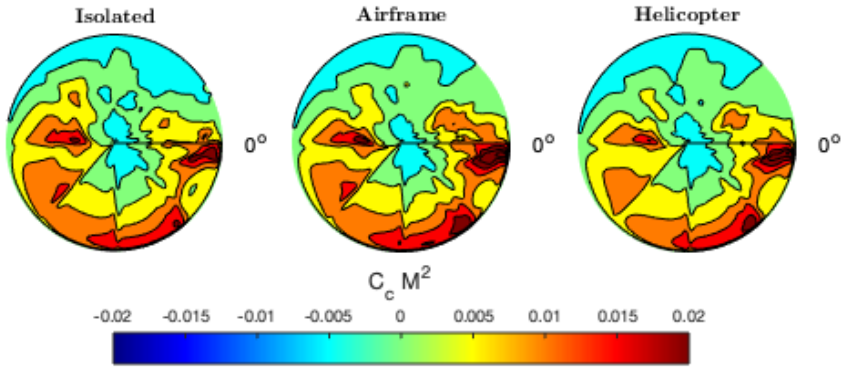

(b) Chordwise Force

Figure 4.1: Aerodynamic Interaction Effects on Upper Rotor

isolation, the presence of the lower rotor results in an unsteadiness in the normal force along the upper rotor and a drop off in normal force every 45 degrees when

the rotor blades cross. Including the airframe in the CFD simulations results in an increase in normal force along the advancing side due to the increase in θ_{1C}. The inclusion of the propeller shows a slight decrease in normal force along the entire disk.

Figure 4.1b shows the non-dimensional azimuthal chordwise force distribution, in the airfoil frame, for the various configurations. The chordwise force is defined as positive from trailing edge to leading edge in the airfoil frame. Note the unsteadiness seen in the normal force is also found in the chordwise force with distinct lines every 45 degrees on the retreating side. This unsteadiness is due to the proximity between the upper rotor blades and the lower rotor wake [9]. At this forward flight speed, the rotor disk is tilted aft increasing wake interactions as evidenced in Figure 4.3. Including the airframe in the CFD simulation results in the chordwise force increasing along the entire disk, most notably near 0 degrees when the blades cross the tail. The presence of the propeller in the full configuration slightly decreases the aft chordwise force but does not show significant effect elsewhere.

4.3 Interactional Aerodynamics Affecting the Lower Rotor

This section will focus on the aerodynamic interactions affecting the lower rotor that arise when analyzing the coaxial rotor in isolation as well as in conjunction with the airframe and full vehicle.

Figure 4.2a shows the non-dimensional azimuthal normal force distribution for the various configurations (ψ=0 on right side). Note that the lower rotor rotates in

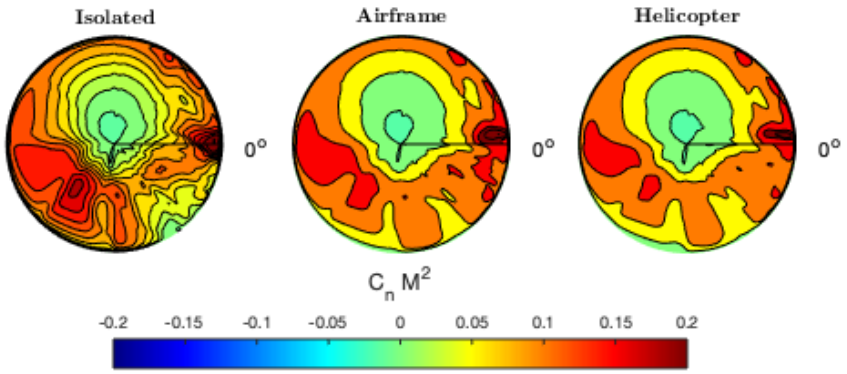

(a) Normal Force

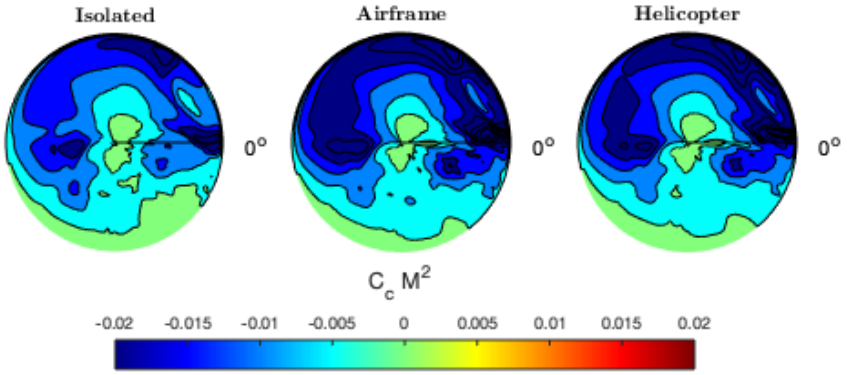

(b) Chordwise Force

Figure 4.2: Aerodynamic Interaction Effects on Lower Rotor

a clockwise manner. The presence of the upper rotor in the CFD simulation causes a loss in normal force every 45 degrees along the advancing side starting at midspan of the blade and extending to the tip [9]. This decrease in normal force is a function of the blade crossing because the pressure on the top side of the lower rotor blade increases as the upper rotor passes the lower rotor. When the airframe is included in the CFD simulation, the normal force along the front of the rotor disk is increased due to the upwash from the fuselage [9]. Moreover, there is an increase in normal force at the aft portion of the rotor disk as the lower rotor blades pass over the fuselage. Including the propeller in the CFD simulation reduces the effect of the

fuselage tail on the aft portion of the rotor disk but has little effect elsewhere.

Figure 4.2b shows the non-dimensional azimuthal chordwise force distribution, in the airfoil frame, for the various configurations. The chordwise force is defined as positive from trailing edge to leading edge in the airfoil frame. Including the airframe in the CFD simulation results in not only decreased chordwise force along the entire rotor disk but also an increased unsteadiness along the aft portion of the disk. This unsteadiness is a result of the lower rotor interacting with the wake from the mast [9]. The addition of the propeller does not result in a significant difference from the airframe case.

Both coaxial rotors experience greater fluctuations in airloads using CFD to model the aerodynamics compared to MFW. The free wake model is capable of capturing some blade crossing interactions but does not capture any of the high airloads near the tail that are seen in the CFD results. Figure 4.3 presents a side view of the predicted wake propagation for both models to better understand this discrepancy in airloads. Note that the fuselage and propeller were not modeled in the free wake but were included in the figure to provide context for the propagation of the wake.

The MFW results show that the wake trailers stay in the plane of their producing rotor due to the high flight speed. This would be the cause of the unsteadiness along the advancing side of the free wake airloads. Furthermore, the wake from both rotors has a slight vertical velocity down which causes the upper rotor wake (blue) to interact with the lower rotor. This would lead to the higher airloads on the lower rotor for the free wake model.

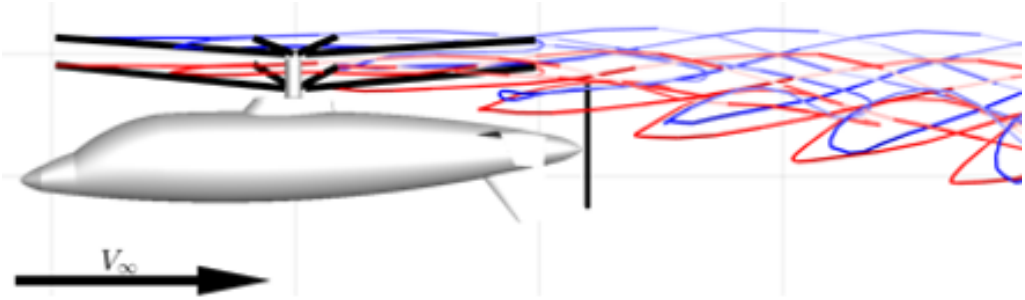

(a) MFW

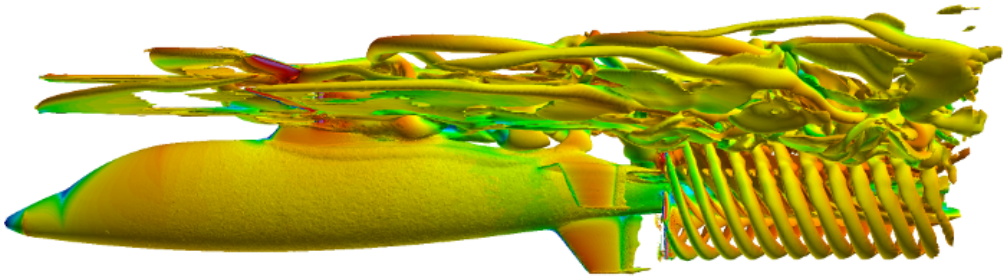

(b) CFD

Figure 4.3: Side View of Coaxial Rotor Wake Propagation

Conversely, the wake in the CFD model has a slight vertical velocity up which is evident in the tip vortex from the leading lower blade. This is caused by the slight shaft tilt backwards from the trim condition. This means that the upper rotor will partially slice through the wake of the lower rotor which would explain the peaking around ψ=0 on the upper rotor airloads. These wake interactions create a messy flowfield around the coaxial rotors and unsteady wake that is partially ingested by the propeller.

4.4 Interactional Aerodynamics Affecting the Pusher Propeller

This section will examine the effects of the helicopter components on the pusher propeller aerodynamic forces. The pusher propeller rotates counter-clockwise,

with ψ=0 degrees at the top and ψ=90 degrees on the starboard side of the helicopter (left side of the plot).

Figure 4.4a shows the non-dimensional azimuthal normal force distribution for the various configurations. The propeller in isolation produces smooth asymmetrical normal force over the disk with the advancing side generating more normal force than the retreating side. This imbalance of normal force is caused by the vehicle pitch which is nose up at 150 knots. The incoming flow comes at a slight angle of attack instead of normal to the propeller disk. On the advancing side of the disk,

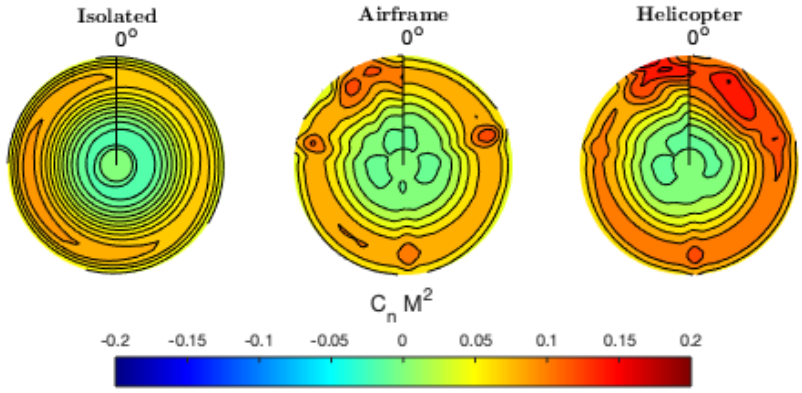

(a) Normal Force

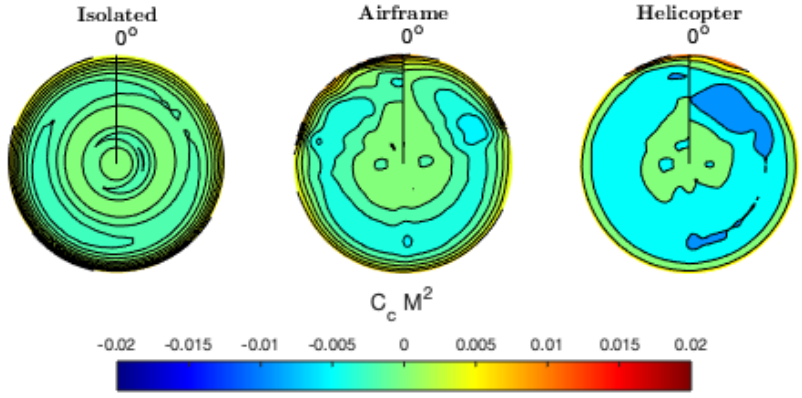

(b) Chordwise Force

Figure 4.4: Aerodynamic Interaction Effects on Pusher Propeller

the edgewise velocity of the propeller disk is compounded with rotational velocity resulting in greater normal force. Conversely on the retreating side, the edgewise velocity of the propeller disk is subtracted from the rotational velocity, lowering the normal force.

Including the airframe in the CFD simulation results in an increase in normal force over the entire propeller disk with the most prominent change occurring at 0 degrees azimuth. The increase along the inboard sections of the disk is a result of the propeller ingesting the wake from the fuselage. The angle of attack on the inboard stations of an isolated propeller is low due to the high inflow velocity which is approximately the forward flight speed. The wake from the fuselage lowers the inflow velocity at these inboard stations; thereby, increasing the angle of attack and normal force. The four distinct spikes in normal force correspond to the wake from the pylon/mast (ψ =0°), horizontal (ψ =90° and (ψ =270°) and vertical (ψ =180°) tails interacting with the propeller. Furthermore, when the entire helicopter configuration is modeled there is an even greater increase in normal force along the outboard sections of the propeller disk, particularly the upper half. The coaxial rotor wake is now propagating backward across the fuselage and then ingested by the propeller. The ingestion of the coaxial rotor wake causes the large unsteadiness observed around ψ=0°. The increase in normal force is due to a phenomenon known as boundary layer ingestion, which has been studied extensively by Min et al. in Ref. [18].

Chapter 5: Acoustic Results

5.1 Isolated Components Case

The normal and chordwise forces, $C_N M^2$, and $C_C M^2$ were obtained from the surface data in Helios at 40 spanwise locations along the blade which were then used as inputs into ACUM then converted to pressure fluctuations through the FWH equation. Each component (upper rotor, lower rotor, and propeller) was analyzed in ACUM individually at the same observer locations so they could accurately be compared. As seen in Section 4, there are significant aerodynamic interactions between components. In order to quantify these interactional effects on the acoustic predictions, the isolated case serves as a baseline. As discussed in Chapter 2, observer locations were placed in a 80 ft hemisphere below the rotor at $\Delta 10^o$ in elevation and $\Delta 15^o$ in azimuth.

Figure 5.1 shows the pressure signals for one revolution of the main rotor at the maximum noise observer ($\psi = 90^o$, $\theta = 60^o$). As expected for a four-bladed rotor, an obvious 4/rev signal can be seen in Figure 5.1a; however, an 8/rev signal should be similarly noticeable due to the coaxial rotors. It is difficult to analyze the combined signal further because the higher frequencies are seemingly dominated by noise. The components were analyzed in ACUM separately for this reason allowing

for analysis of the independent signals and noise as seen in Figure 5.1b.

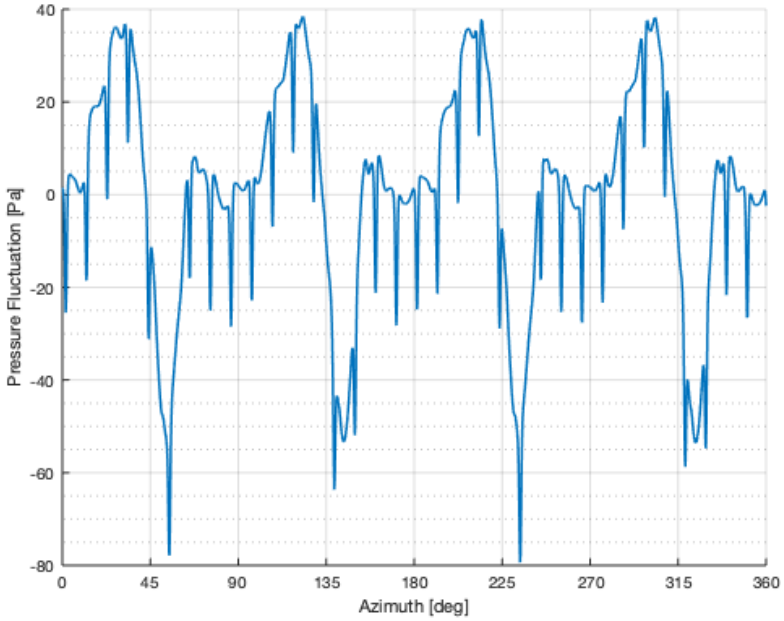

(a) Combined Signal

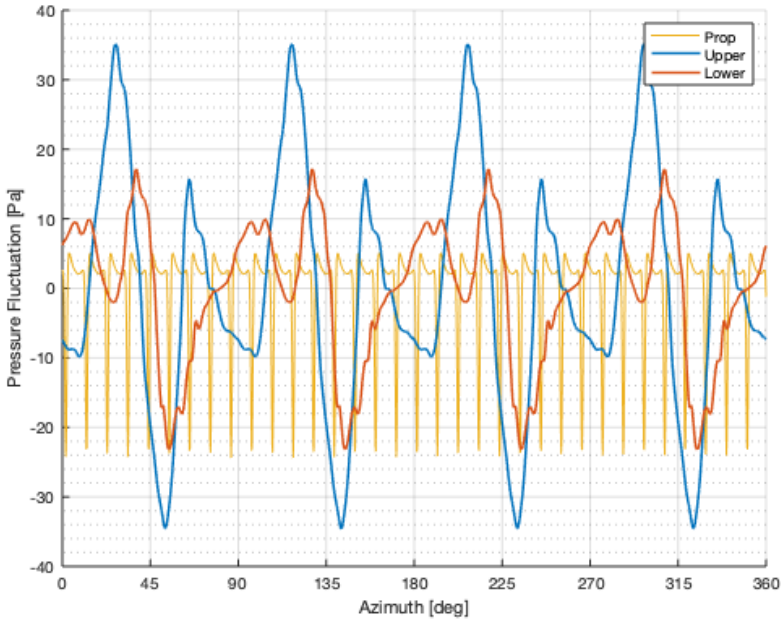

(b) Independent Components

Figure 5.1: Isolated Azimuth Pressure History at Maximum Noise

Figure 5.1b demonstrates the 4/rev signal as well as showing the main rotors are nearly in-phase which explains the lack of a clear 8/rev in the combined signal. The upper rotor is the maximum contributor for pressure at this location, which is unsurprising since this maximum location is at the advancing side of the upper rotor with an expected large loading noise. Moreover, the apparent signal noise is high-frequency contributions from the propeller which spins at an RPM 5.67 times greater than that of the main rotor.

For more detailed spectral analysis, it is necessary to transform the time signal into the frequency domain using FFT. Figure 5.2 shows the dominant frequency is the 8/rev signal from the blade passage of the upper and lower rotors. The propeller

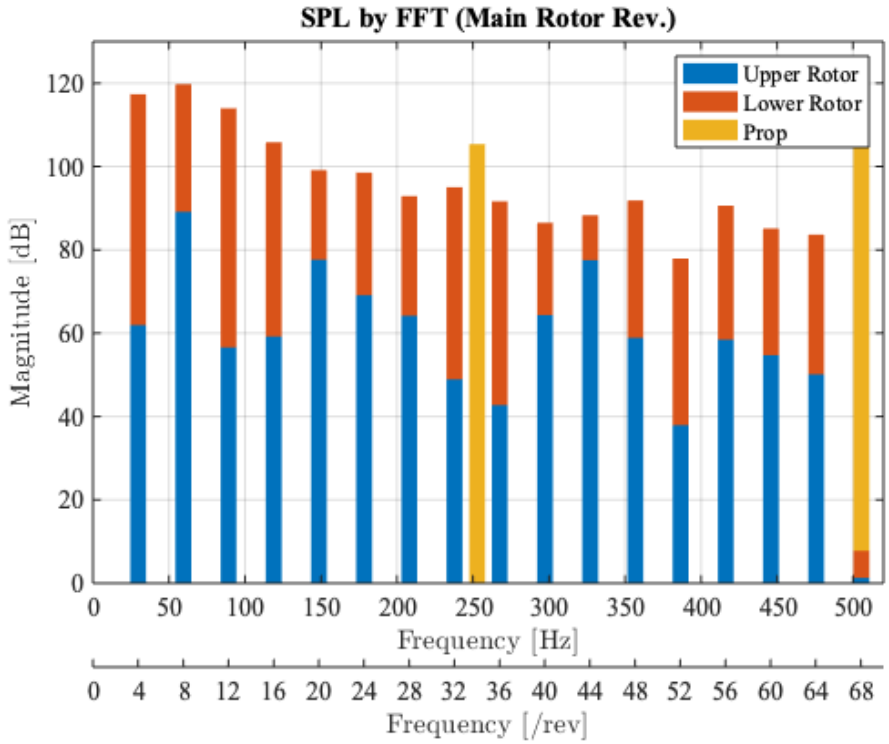

Figure 5.2: SPL of Isolated Components by Frequency

has substantial noise contributions at higher frequency content, namely 250 Hz and 500 Hz or 34 and 68/rev. The /rev x-axis is in terms of the coaxial rotor revolutions so the 34/rev would be the 1st frequency for the propeller when considering the 6 blades and an RPM ratio of 5.67 compared to the coaxial rotors. Overall, the FFT analysis confirms that the main rotors dominate the low frequencies; however, it also shows that at higher frequencies the propeller provides substantial noise contributions which are not immediately evident in the time and pressure domain. This discrepancy in dominant frequencies is evidence that examining the A-weighting is crucial. It is critical to examine the observer hemispheres from not only the dB SPL but also the dBA SPL to have a greater understanding of the overall noise.

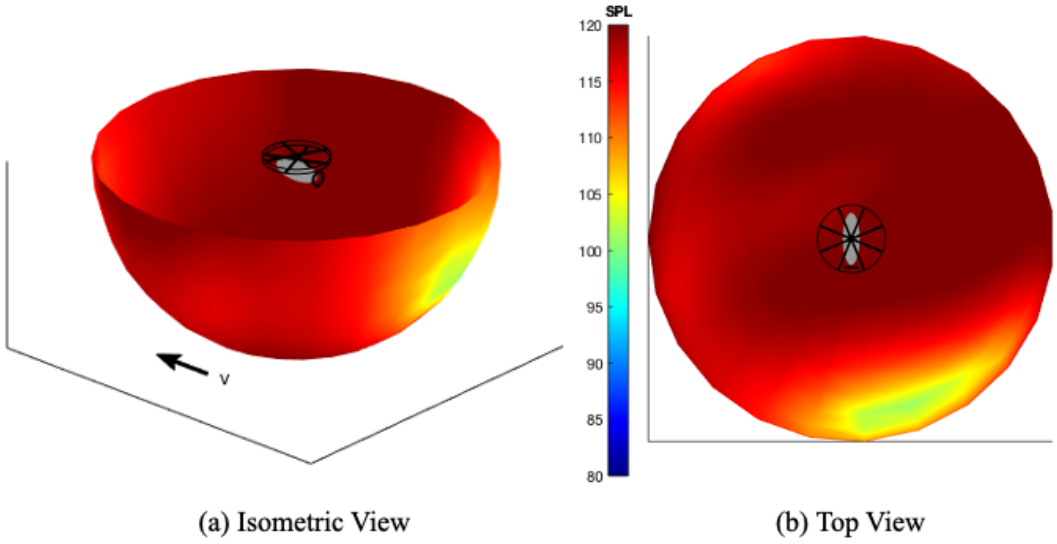

Figure 5.3: Hemisphere of Isolated Total SPL

The observer hemispheres provide a more complete understanding of the distribution of noise. The observer hemispheres are three dimensional which allows for

different vantage points as seen in Figure 5.3. The isometric view provides greater detail of the vertical depth of the observer bowl but the top view shows azimuthal variations in greater clarity. Because there is more azimuth clarity, the top down view will be used extensively in this thesis with the understanding that it extends in the z dimension.

Figures 5.4 and 5.5 show the SPL in dB and A-weighted dB (dBA) respectively of the upper rotor, lower rotor, and propeller individually as well as the combined total noise. Figure 5.4a and 5.4b focus on the noise solely from the pressure fluctuations on the upper rotor blades and lower rotor blades. Due to the flight conditions

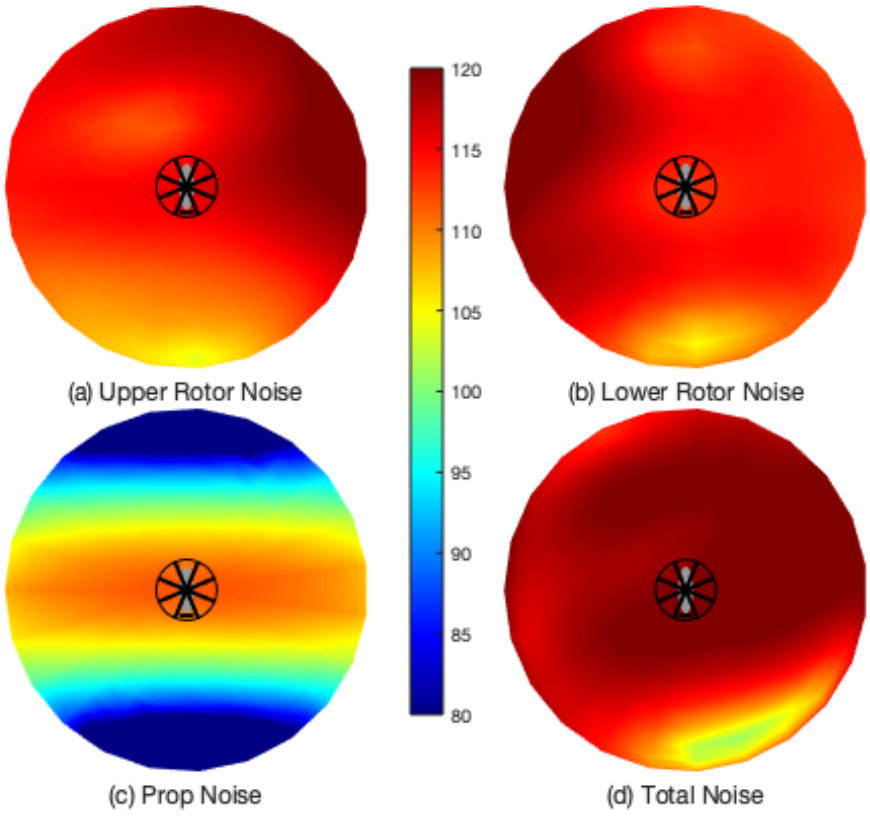

Figure 5.4: SPL of Isolated Components and Total SPL in dB

and tip mach, it is expected that the main rotors would be dominated by loading noise. This would be supported by the increase in noise on the advancing side of both blades. Another area of interest would be ψ=0, where a quieter pocket can be observed on both rotor disks.

This low point is observed in both main rotors as well as the total rotor noise. This could simply be a function of the trim state; however, as discussed in Section 4.2, the wake is nearly parallel to the rotor disk at this flight condition. Therefore, this could be an effect of blade interactions with each other or the wake.

On the other hand, the propeller contour (Figure 5.4c) shows a single band of noise directly under the propeller that gets drastically weaker as the observer gets out from underneath the helicopter. Unlike the main rotors, this banding effect would suggest that the propeller is dominated by thickness noise instead of loading. The lack of loading noise is largely dependent upon the chosen flight condition and the proposed use of the propeller. The purpose of this flight condition is to provide a greater forward thrust to counter-act the fuselage drag. This amount of thrust is going to be less than the vertical thrust needed to counter the weight of the helicopter. Furthermore, the propeller is receiving nearly axisymmetric undisturbed inflow which creates a near steady-state environment. The large thickness noise coincides with the large twist present in the nominal propeller blades.

As expected from the time history and FFT analysis, the total noise (Figure 5.4d) is dominated by the main rotors with little evidence of any propeller influence. The total noise hemisphere shows a simple combination of the high advancing side noise from both rotors causing most observers to experience nearly 120 dB of noise.

The propeller max is around 110 dB meaning it would be heard half as loud as the main rotors. However, the main rotors command over total noise does not extend to the A-weighted dB.

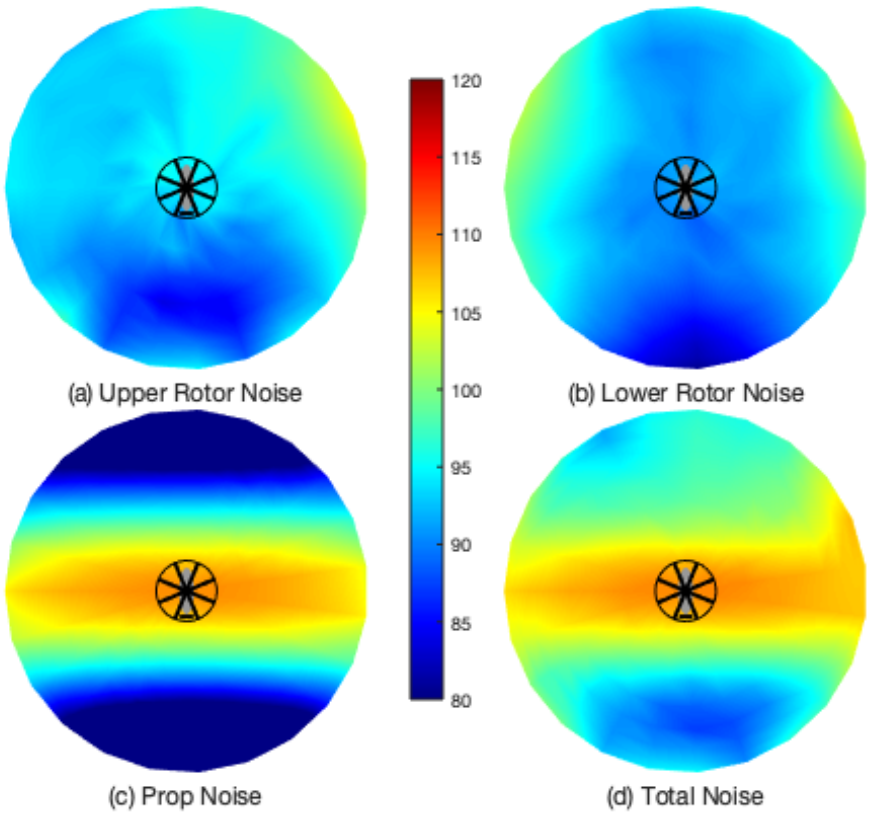

Figure 5.5: SPL of Isolated Components and Total SPL in dBA

The dBA contours shown in Figure 5.5 vastly differ from those shown above. The primary differences are in the main rotor and total noise contours. The main rotors principal frequencies are less than 100 Hz resulting in a -20 to -40 dB change from the A-weighting curve (Figure 2.7). This results in a much softer SPL from the main rotors and also highlights the high-frequency noise sources of the propeller. The propeller's dominant frequencies are all greater than 250 Hz resulting in a much

lower dB reduction. This is confirmed in Table 5.1, which shows the OASPL in both dB and dBA. This would indicate that the observers might hear a smaller amount of noise from the propeller but would find it more irritating based on the frequency of the noise.

Table 5.1: OASPL for Isolated Components

Component	**OASPL (dB)**	**OASPL (dBA)**
Upper Rotor	117.4	92.7
Lower Rotor	113.9	91.4
Propeller	111.2	108.9
Total	121.33	109.0

Overall, the trends seen for the main rotors are consistent between the dB and dBA contours. However, the lower rotor shows a louder spot on its retreating side (Figure 5.5b). This signals the presence of higher frequency content along portions of the lower rotor that has a greater effect on thickness noise based on the high elevation of the observers. The high-frequency content could indicate an increase in blade-vortex interactions (BVI) between the advancing upper rotor and retreating lower rotor.

There is little change in the propeller contour which is expected as it operates at a much higher frequency than the main rotor resulting in a lower dB adjustment. Moreover, the propeller for the isolated case operates in a clean flow environment so there should not be any hidden frequency content as observed with the main rotors.

The isolated components simulations were able to capture some aerodynamic interaction effects between the main rotors which was anticipated because the main

rotor system was simulated in CFD together. However, the propeller demonstrated nominal thickness dominated acoustics. While this could provide a baseline prediction of the acoustics, it is expected that the propeller acoustic contour will change when including the airframe and full configuration as the interactions upstream of the propeller will remove the clean inflow.

5.2 Airframe Components Case

The airframe simulations were conducted in Helios with the same parameters as the isolated simulations above except including the nominal fuselage within the CFD simulation. The simulations were split into the main rotor system and nominal fuselage, and the propeller and nominal fuselage. The inputs into the ACUM code were kept constant in between the different cases except that normal and chordwise forces were pulled from the airframe simulations.

Figure 5.6 shows the pressure signals for one revolution of the main rotor at the maximum noise observer (ψ=90°, θ=60°). It is unclear from Figure 5.6a whether adding the fuselage altered the pressure fluctuations of the main rotor. Comparing Figures 5.1b and 5.6b, it can be seen that there is a noticeable amplitude decrease for the upper and lower rotors. However, the signal in both Figure 5.6a and 5.6b shows an amplitude increase in the high-frequency propeller pressure fluctuations which was expected based on the aerodynamic impact seen in Section 4.4. The pressure signal only examines the maximum noise observer location so to understand the full effect of the fuselage it is necessary to investigate the entire observer hemisphere.

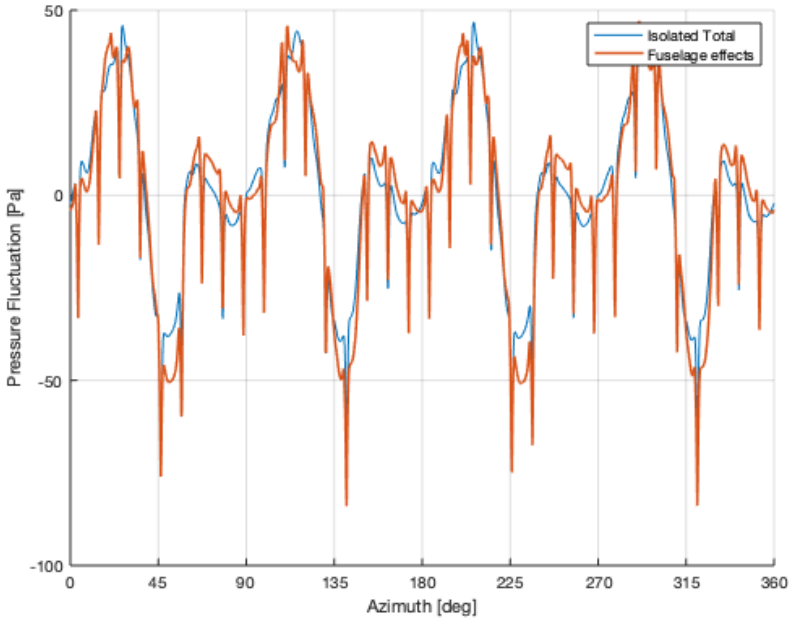

(a) Combined Signal of Isolated and Airframe

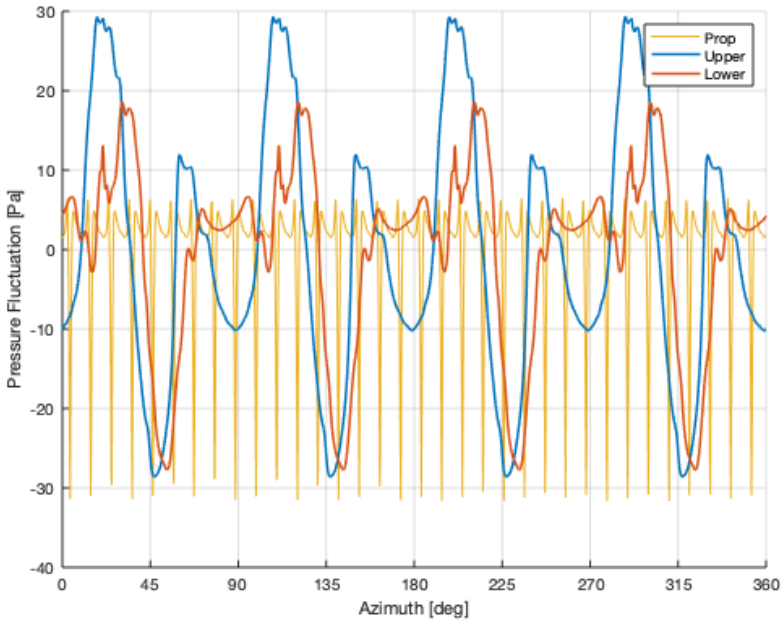

(b) Independent Components of Airframe

Figure 5.6: Airframe Azimuth Pressure History at Maximum Noise

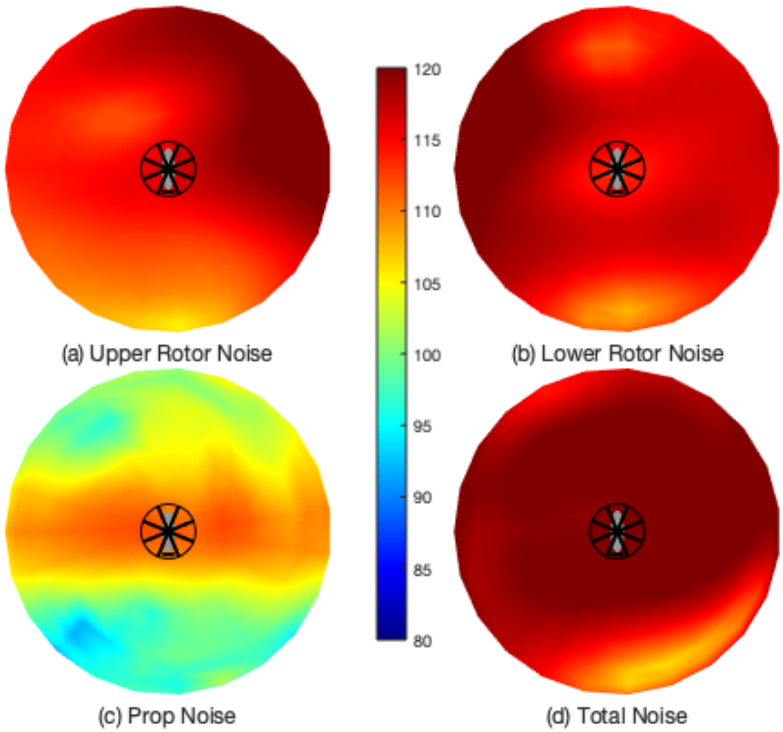

Figure 5.7: SPL of Airframe Case Components and Total in dB

When examining the observer hemispheres in Figure 5.7, the most obvious effect from the airframe is on the propeller. The isolated propeller was entirely dominated by thickness noise directly underneath with bands of decreasing noise outwards. The airframe propeller noise still has the prominent thickness noise underneath the propeller but the presence of the fuselage has diffused the noise throughout the entire hemisphere. A surprising effect of the fuselage on the propeller noise is the propagation of noise further upstream. From the upper half of the hemisphere (Quadrant 2-3), it would seem that observers in of front the fuselage and propeller would hear a greater amount of noise than those behind the propeller. In order to see this effect more clearly, the isometric view of the airframe propeller noise is

shown in Figure 5.8. The observers proceeding the propeller hear a greater portion

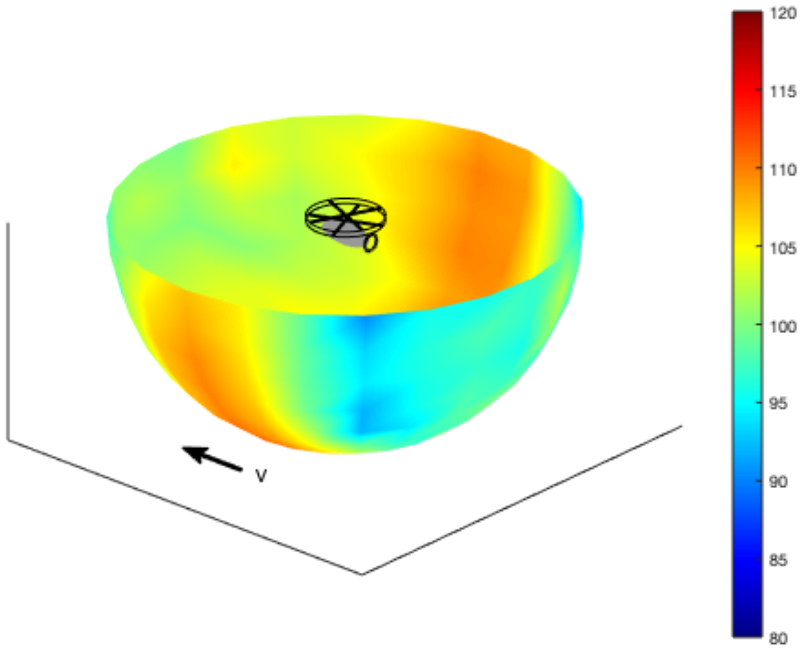

Figure 5.8: Isometric View of Airframe Propeller Hemisphere

of the noise compared to those following. This diffusion of noise from the propeller would indicate that the presence of the airframe upstream is having a drastic impact on the loading noise of the propeller. This is further supported by the noticeable increase in normal force along the propeller as a consequence of the boundary layer ingestion phenomena discussed in Section 4.4 and shown in the propeller airloads (Figure 4.4). However, the increased loading noise is expected to have a greater effect behind the propeller rather than in front unlike what is being observed. It is unclear the exact cause of the diffusion of propeller noise but including the fuselage in the propeller simulation causes a greater number of observers to experience a

considerable increase in high-frequency noise.

Unlike the propeller, the fuselage effects on the main rotors are less pronounced. The SPL difference between the airframe and isolated cases was calculated for all observers and shown in Figure 5.9 to provide greater clarity. Similar to the airloads, the upper rotor shows little difference in noise between the isolated and airframe cases. However, the lower rotor is showing a greater effect from the airframe with an increase on the retreating side compared to the isolated case. The changes seem relatively minor (+3-6 dB) compared to the total noise of 120 dB but this is a large enough that observers would notice the increase in noise. Note the difference at the forward and backward extremes for the propeller is +40dB; however, Figure

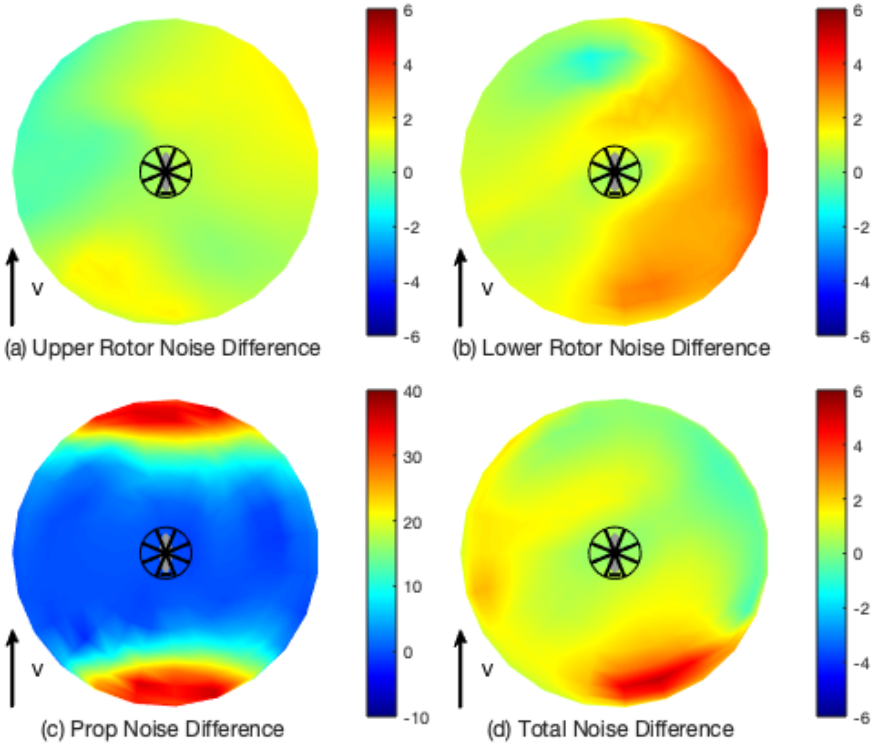

Figure 5.9: SPL of Difference between Airframe and Isolated Cases in dB

5.8 shows these locations ∼100 dB. The isolated propeller SPL at these extremes was much lower than 80 dB in the isolated case (∼ 60 dB). The airframe case raised the SPL of the propeller in these locations into the comparable threshold of the main rotors. Between the lower rotor noise increase and the drastic propeller noise change, the total noise from the helicopter rises between 2 and 6 dB for observers underneath and downstream as seen in Figure 5.9d.

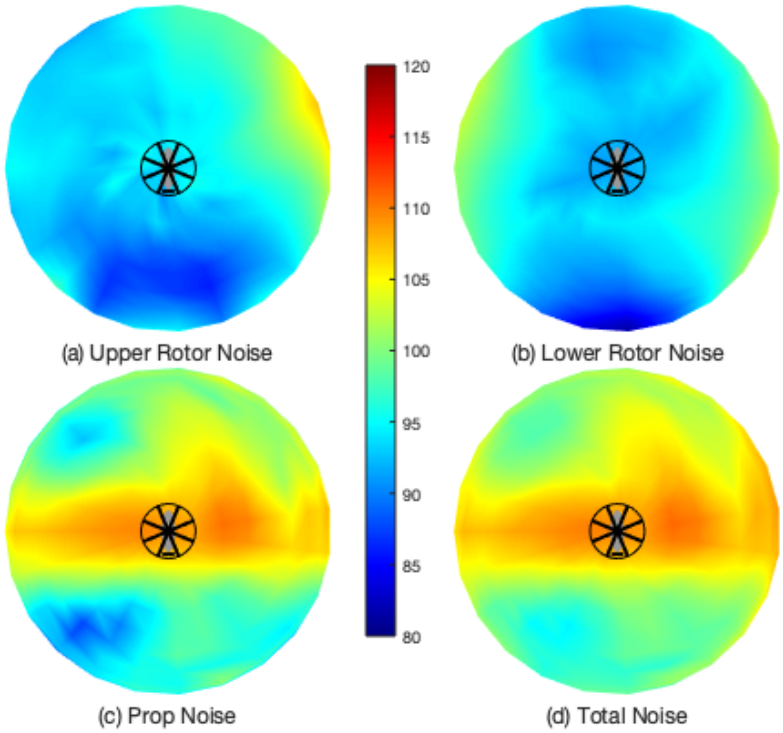

Figure 5.10: SPL of Airframe Components and Total in dBA

The fuselage had an even greater effect on A-weighted dB for all of the components as seen in Figure 5.10 and 5.11 (Note: color scale is larger for dBA difference). Figure 5.10 shows a similar trend to the isolated case with the propeller dominating the total rotor noise except that the noise is less banded; thereby, affecting a greater

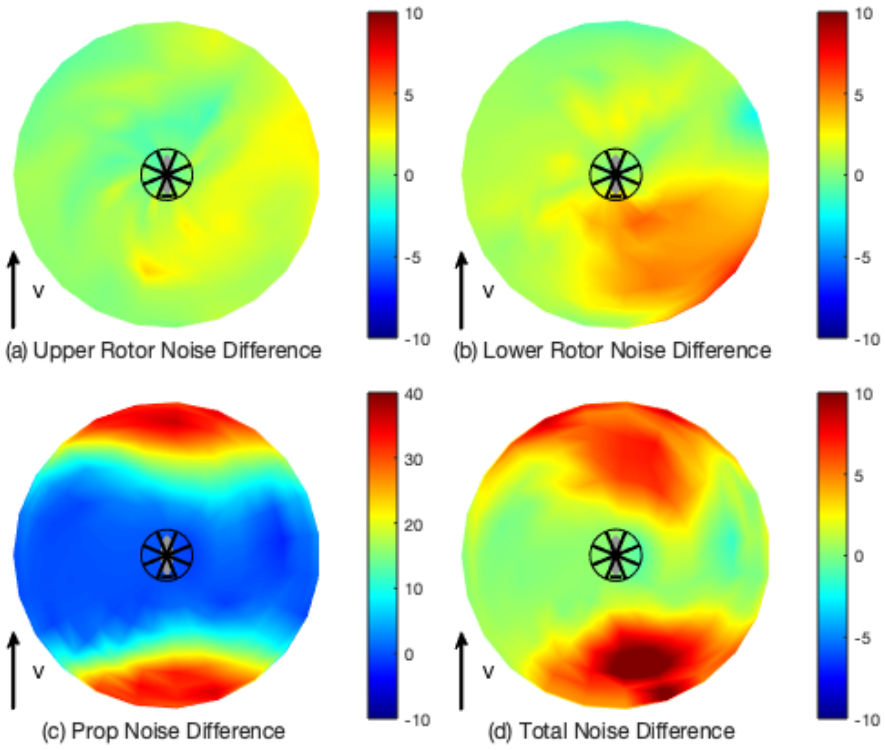

Figure 5.11: SPL of Difference Between Airframe and Isolated in dBA

amount of observers. The propeller difference (Figure 5.11c) follows the same trend between dB and dBA which is expected considering the frequency content of the propeller which causes it to be weighted less heavily. The main trend difference is total rotor noise which shows a greater number of observers experiencing an increase between 5 and 10 dBA compared to the 3 to 6 dB increase in Figure 5.9d. This can be mostly attributed to the diffusion of propeller noise but there is a significant increase in portions of the lower rotor hemisphere. The large area of 10 dBA increase would indicate observers in this area would experience a doubling of high-frequency noise compared to the isolated case.

The presence of the fuselage had a pronounced effect on the propeller and lower

rotor with negligible changes to the upper rotor acoustic hemisphere. The fuselage caused the noise from the propeller to diffuse within the entire observer hemisphere instead of being concentrated in thickness bands seen in the Isolated case. This

Table 5.2: OASPL for Airframe Components with Difference from Isolated Case

Component	**OASPL (dB) [Δ]**	**OASPL (dBA) [Δ]**
Upper Rotor	118.0 [+0.6]	92.9 [+0.2]
Lower Rotor	115.3 [+1.4]	93.9 [+2.5]
Propeller	111.8 [+0.6]	109.9 [+1.0]
Total	122.2 [+0.9]	110.3 [+1.3]

effect is seen clearly in both dB (Figure 5.7c) and dBA (Figure 5.11c). Conversely, the fuselage does not have a drastic effect on the OASPL experience at the maximum observer point as indicated in Table 5.2. This is because that the maximum observer location is underneath the coaxial rotors and within the propeller noise bands. While the noise increase heard from the maximum observer is negligible, Figures 5.9 and 5.11 show that a larger number of observers are experiencing an increase in noise when the fuselage is included in the CFD analysis. While the dB increase seems small enough that it might be unnoticeable, an increase of 3 dB is noticeable and an increase of 10 dB is perceived twice as loud to the human ear. Therefore, the increase in total rotor noise is detectable by the majority of observers and almost twice as loud for those downstream of the helicopter. It is unclear whether the difference in noise will be significant when the full configuration is included in the CFD simulation.

5.3 Full Helicopter Configuration

The helicopter configuration simulation was conducted in Helios with the same parameters as the isolated simulation following the full CSD/CFD coupling described in Section 2.2.4. The main rotor, fuselage, and propeller were all analyzed within the simulation to examine the full aerodynamic interactions between them.

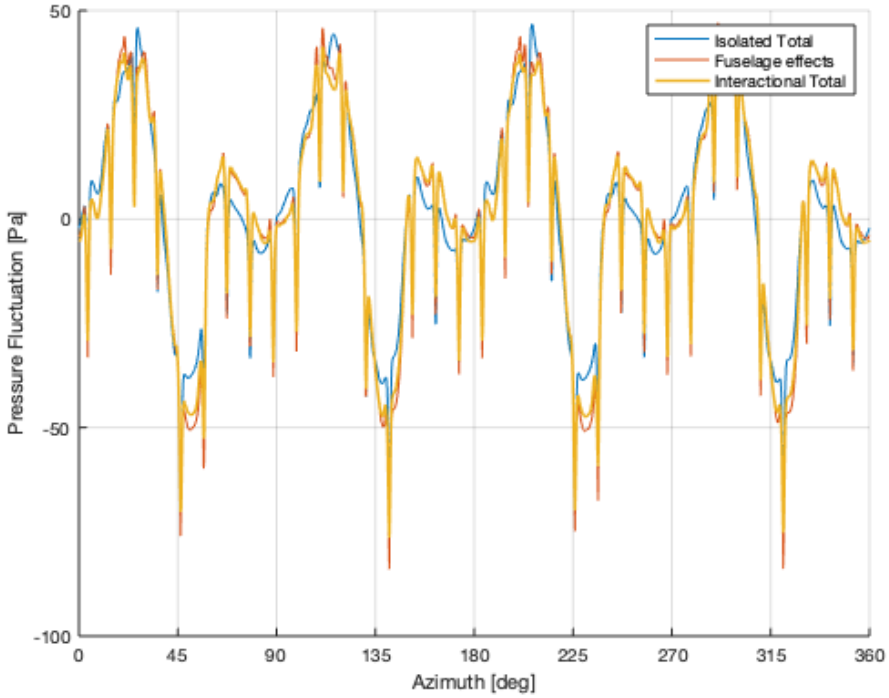

Figure 5.12: Helicopter Azimuth Pressure History at Maximum Noise

There is little difference between the azimuth pressure history of the fuselage and full helicopter at the maximum noise location as seen in Figure 5.12. Both the main rotor low frequencies and the propeller high-frequencies are nearly identical between the helicopter and airframe signals. While it is expected that the full

configuration will have an impact on the propeller, the main impact on the main rotors was the presence of the fuselage which was already captured in the previous airframe simulation.

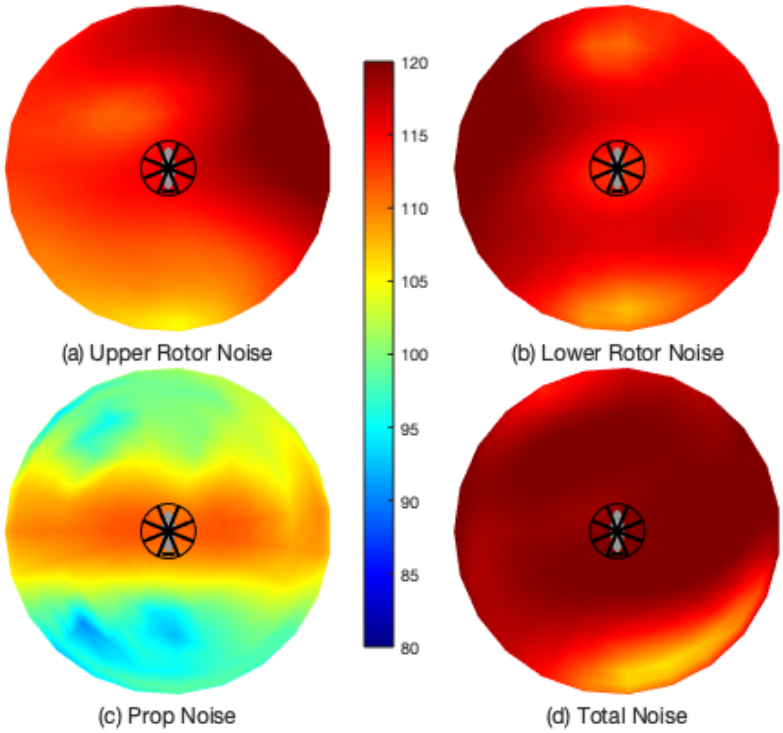

Figure 5.13: SPL of Helicopter Components and Total in dB

Similar to the azimuth pressure history, the hemispheres closely resemble the fuselage simulation except for the propeller (Figure 5.13). The propeller hemisphere displays more banding comparable to the isolated components versus the more diffused noise seen in the airframe case. This greater banding compared to the airframe case results in a total noise hemisphere almost entirely of 120 dB noise (Figure 5.13d). For a clearer view, it is necessary to examine the hemisphere noise differences between both helicopter and isolated as well as helicopter and fuselage

cases. The helicopter-isolated differences (Figure 5.14) presents similar trends as the airframe-isolated differences (Figure 5.9) except with differing magnitudes. The full configuration actually has a slightly lower effect ($\sim$ 1dB) on the upper rotor compared to the pure fuselage (Figure 5.14a and Figure 5.15a) . This could indicate the presence of the propeller reduces the fuselage effect on the upper rotor; however, it is difficult to tell because the effect is so small in magnitude. Overall, the total noise of the full helicopter configuration shows a slight decrease in dB compared to the airframe case; however, this change is so small that it is negligible.

The propeller noise difference between the full helicopter configuration and the airframe, shown in Figure 5.15c, presents peaks at the relative 45° location in each

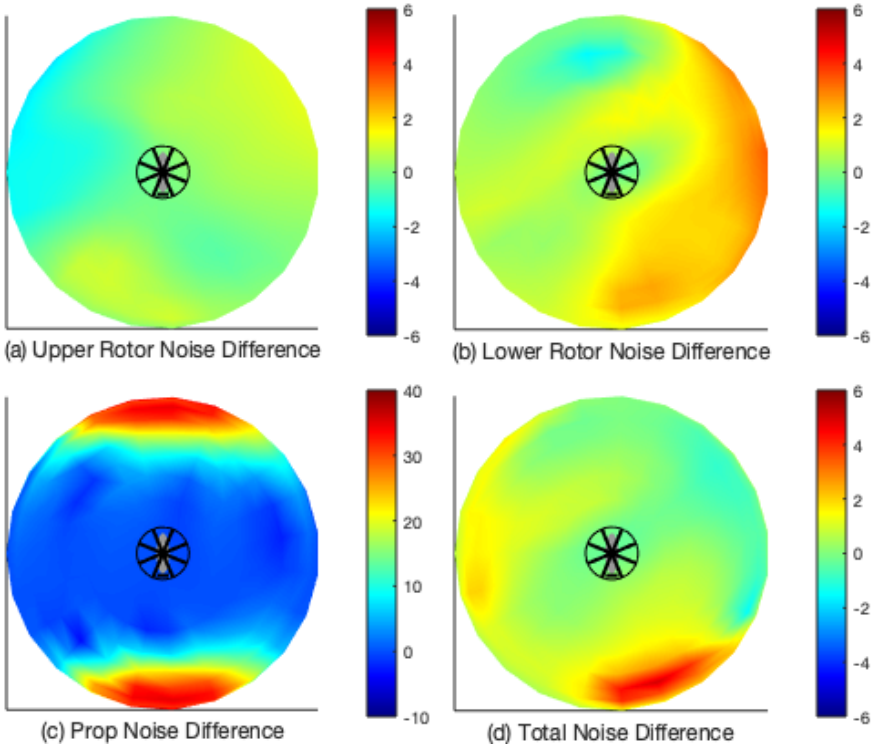

Figure 5.14: SPL of Difference of Full Helicopter v. Isolated in dB

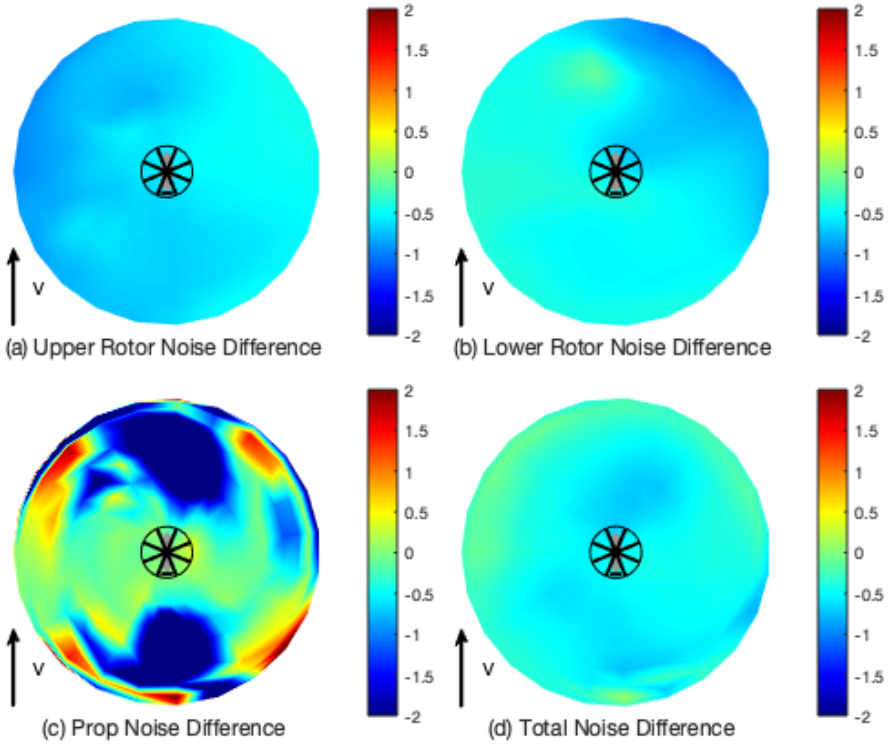

Figure 5.15: SPL of Difference of Full Helicopter v. Airframe in dB

quadrant (ψ=45 deg, 135 deg, 225 deg, 315 deg). The location of these peaks could indicate an increase in loading noise from the propeller as the shape models that of the nominal loading noise. This is most likely caused by the unsteady wake from the main rotor system getting ingested by the propeller. This results in portions of the propeller disk producing a greater amount of normal force than before causing an increase in some observer noise and portions producing less force reducing the noise heard by certain observers.

The dBA hemispheres of the full helicopter configuration shown in Figure 5.16 display little difference in the coaxial rotors compared to the airframe configuration as seen in Figure 5.18. The propeller dBA has less banding than that seen in

the full configuration dB especially near $\psi = 90$ deg. The total rotor noise in dBA is dominated by the propeller as expected but demonstrates less noise directly upstream and downstream of the helicopter compared to the airframe case. This is further supported by the dBA decrease in the propeller and total rotor noise upstream and downstream of the helicopter shown in Figure 5.18c and 5.18d.

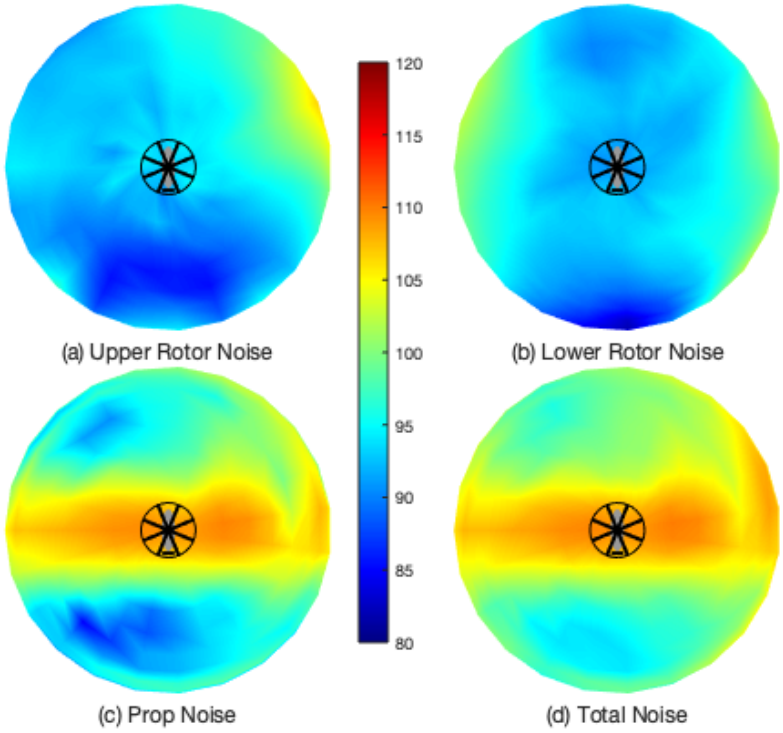

Figure 5.16: SPL of Helicopter Components and Total in dBA

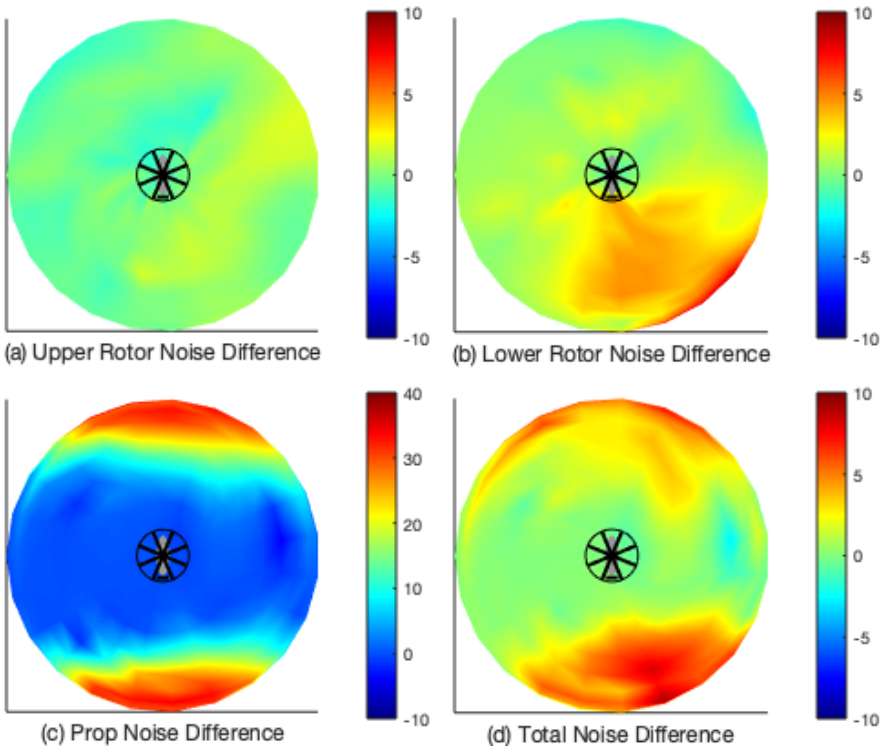

Figure 5.17: SPL of Difference of Full Helicopter v. Isolated in dBA

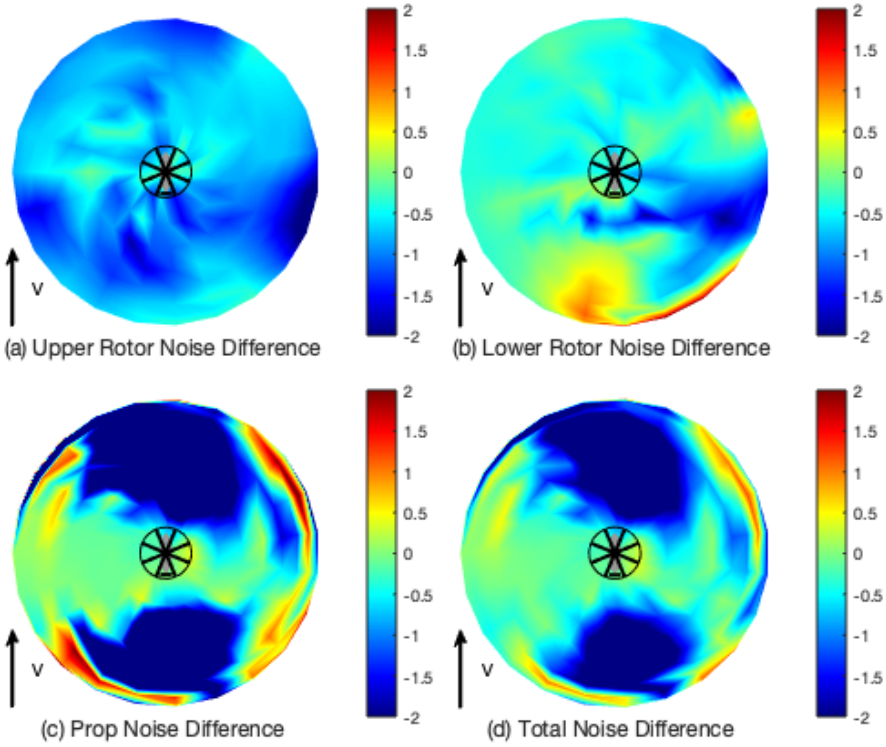

Figure 5.18: SPL of Difference of Full Helicopter v. Airframe in dBA

The upper rotor hemispheres in Figures 5.17a and 5.18a shows little change from the isolated case and negates some of the observer noise changes originally seen in the airframe case. The changes between the helicopter and airframe case are small enough to be neglected compared to the differences in the lower rotor and propeller. The lower rotor shows a greater increase over the isolated case but still negates some of the noise changes from the airframe case except around ψ=0 where there is a small increase. These changes in the lower rotor noise mimic those seen in airloads; however, the changes between the airframe case and full configuration are negligible.

As seen with the airframe case, the inclusion of the full helicopter configuration within the CFD and acoustics modifies which observer locations experience a greater amount of noise. The primary effect is on the propeller which experiences a noise increase close to 40 dB for observers for at the upstream and downstream edges of the hemisphere compared to the isolated case. This amounts to a maximum fluctuation of 3 dB (6 dBA) for some observers compared to the airframe case. The difference between the helicopter and airframe cases is large enough to be noticeable to these observers but would not be perceived as twice as loud. The OASPL for

Table 5.3: OASPL for Helicopter Components with Difference from Airframe

Component	**OASPL (dB) [Δ]**	**OASPL (dBA) [Δ]**
Upper Rotor	117.7 [-0.3]	94.0 [+1.0]
Lower Rotor	114.9 [-0.4]	92.9 [-1.0]
Propeller	111.6 [-0.2]	109.5 [-0.4]
Total	121.8 [-0.4]	109.7 [-0.6]

the maximum observer location decreases slightly compared to the airframe case as seen in Table 5.3. This decrease would not be noticeable to the human ear but does provide further support that the presence of the airframe has a greater affect on all components than the full helicopter configuration.

Overall, there were some small differences in noise between the full helicopter configuration and the airframe configuration. These differences were largely negligible especially for the coaxial rotors coinciding with the lack of effect the propeller had on the coaxial rotor aerodynamics. Conversely, the coaxial rotors had a greater effect on the propeller aerodynamics than on the propeller acoustics.

Chapter 6: Conclusions and Future Work

6.1 Interactional Effects on Coaxial Rotor Acoustics

There were only slight changes in the acoustic predictions of the coaxial rotor system between the different cases. This is due, in large part, to the isolated case including both coaxial rotors within the same CFD simulation. Therefore, the majority of the interactions caused by the coaxial rotor system were already included in the isolated case. This resulted in little change in the upper rotor noise between the three configurations. This is evidenced by the acoustic hemisphere for the upper rotor as shown in Figure 6.1. The upper rotor experiences a decent amount of azimuthal change in normal and chordwise forces with the greatest change observed with the inclusion of the airframe. However, these changes do not translate to noise for the upper rotor as the acoustic hemisphere exhibits minimal changes between the different cases.

The lower rotor also shows airload differences between configurations with the greatest change resulting from the addition of the airframe within the CFD simulation (Figure 6.2). Unlike the upper rotor, this has a noticeable impact on the noise experienced by the observers. The observers on the retreating side of the lower rotor experience an increase in noise of about 6 dB. While not quite loud enough

to double the noise, this increase is large enough to be obvious to all of the affected observers.

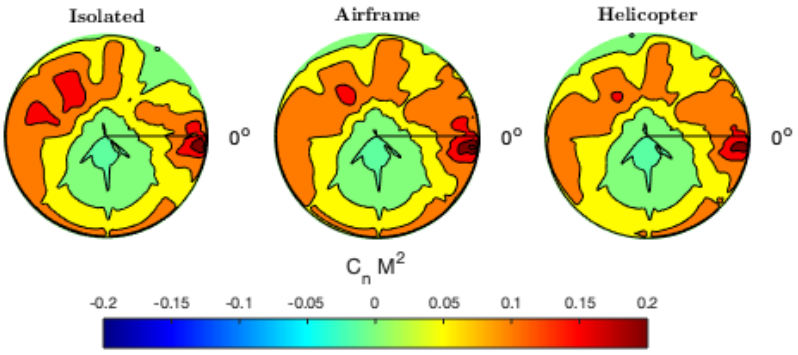

(a) Normal Force

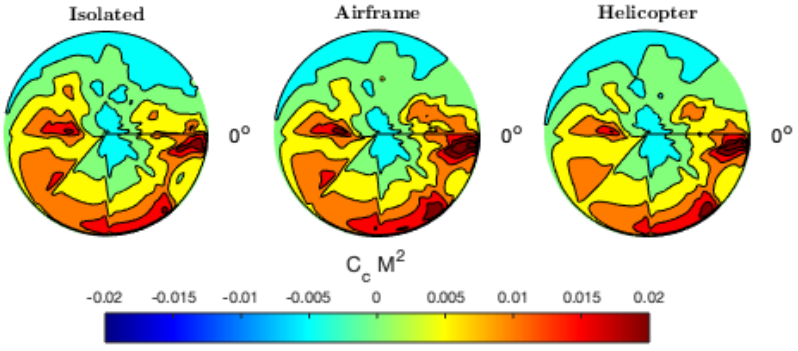

(b) Chordwise Force

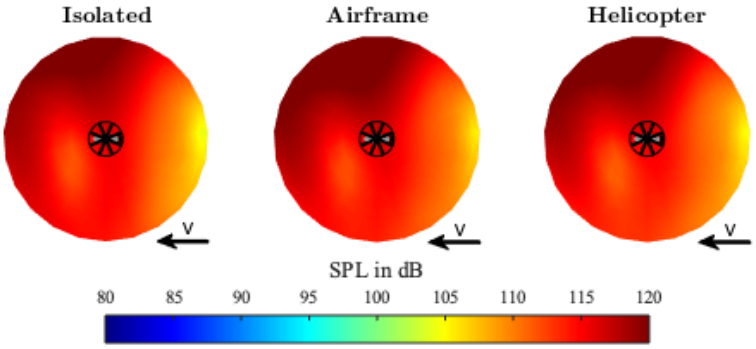

(c) SPL Hemisphere in dB

Figure 6.1: Interaction Effects on Upper Rotor Aerodynamics and Acoustics

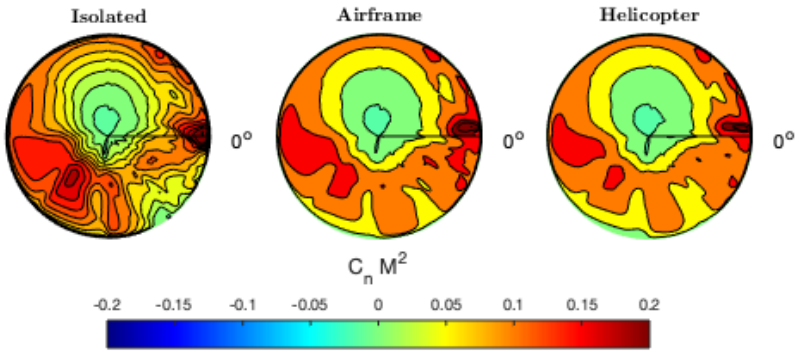

(a) Normal Force

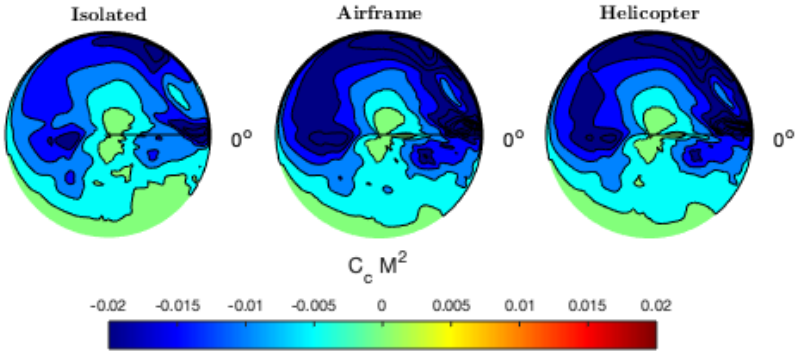

(b) Chordwise Force

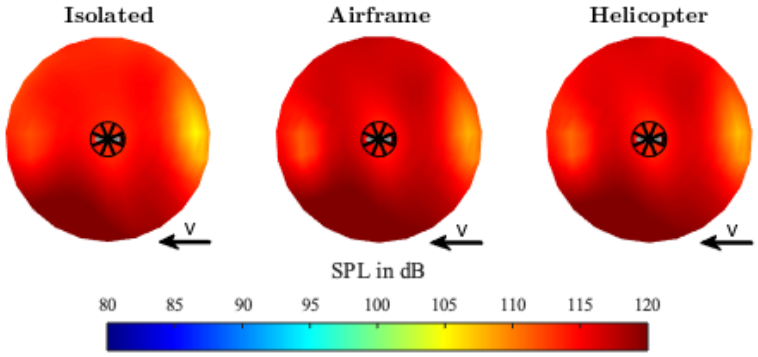

(c) SPL Hemisphere in dB

Figure 6.2: Interaction Effects on Lower Rotor Aerodynamics and Acoustics

It can be concluded that the primary interactions affecting the upper rotor are from the lower rotor resulting in little aerodynamic and acoustic change when including the airframe or full configuration in the CFD simulation. Conversely, the

lower rotor experiences a greater magnitude increase in both normal and chordwise force on the rotor disk from the inclusion of the airframe resulting in a greater amount of noise heard by observers. The full helicopter configuration does not have a substantial impact on the aerodynamics or acoustics compared to the airframe simulation. Therefore, the inclusion of the airframe within the CFD simulation has a non-negligible impact on the acoustic prediction for the lower rotor but the inclusion of the propeller does not have an impact on the coaxial rotor system.

6.2 Interactional Effects on Propeller Acoustics

The propeller experienced the greatest interactional impacts on both aerodynamics and acoustics. The propeller in isolation received nearly steady axisymmetric inflow which resulted in a thickness dominated observer hemisphere shown in Figure 6.3c. The inclusion of the airframe drastically altered both the normal and chordwise forces resulting in a similarly dramatic increase in propeller noise along the upstream and downstream extremes of the observer hemisphere. This increase was between 20-40 dB at these observer locations causing the propeller noise to no longer be negligible compared to the coaxial rotor system. Not only are observers hearing a greater amount of noise than before but they are also subject to the higher frequency of the propeller noise which would cause greater irritation than the coaxial rotor system. Including the full configuration within the CFD simulation causes another $\pm$ 3 dB shift in noise for multiple observers around the hemisphere. The inclusion of the coaxial rotor system with the propeller in the CFD actually lowers

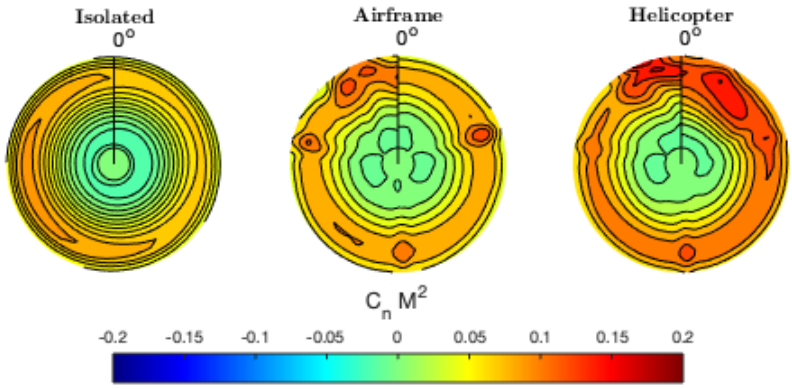

(a) Normal Force

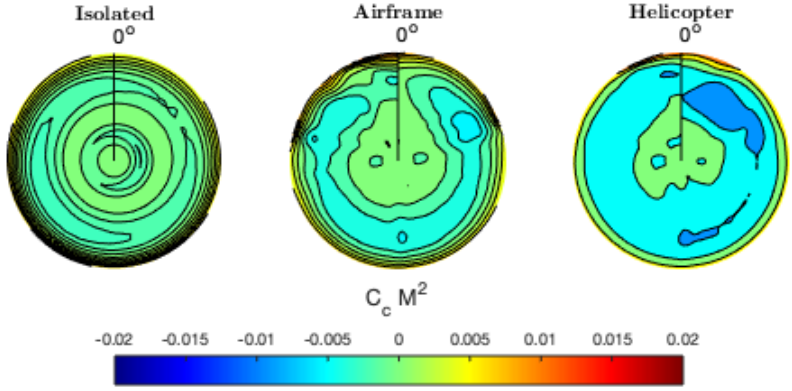

(b) Chordwise Force

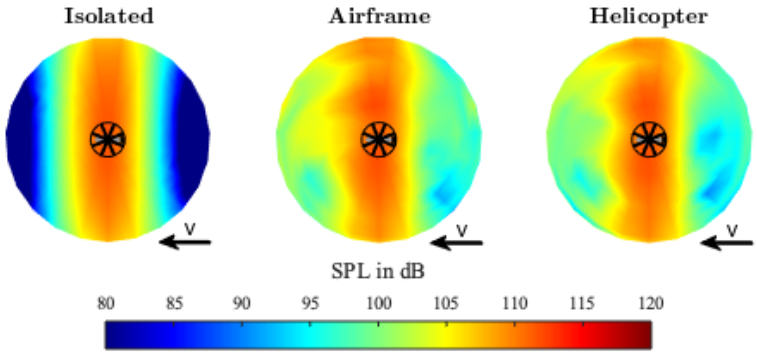

(c) SPL Hemisphere in dB

Figure 6.3: Interaction Effects on Propeller Aerodynamics and Acoustics

the chordwise force at the tip and inboard stations. This could be the cause of the dB reduction downstream of the propeller. While this 3 dB change is large enough

to be noticeable, it is negligible compared to the noise increase across the hemisphere due to the presence of the airframe.

6.3 Conclusions

A computational aeroacoustic framework was developed and implemented successfully for the various helicopter component configurations. The configurations were solved computationally in the CREATE^{TM}-AV Helios framework coupled with PRASADUM to provide a more accurate trim state. The aerodynamic forces were then used as inputs into ACUM to be evaluated in the FWH equation. Observer locations were chosen in a 6 rotor radii ($\sim$ 80 ft) hemisphere underneath the coaxial rotor system and the sources of noise were calculated as pressure fluctuations at each of these locations. An FFT analysis was conducted to break down the pressure time histories into their component frequencies to be summed together. Using the FFT results, an A-weighting analysis was conducted to report noise levels that compensate for the relative loudness of certain frequencies to the human ear.

These calculations were done for three configurations: isolated, airframe, and full helicopter. The isolated configuration analyzed the coaxial rotor system and propeller alone. The airframe configuration analyzed the coaxial rotor system and propeller along with the fuselage, horizontal and vertical stabilizers, pylon, and mast. Finally, the full helicopter configuration analyzed all three components together in a CFD simulation. The primary conclusions drawn from this thesis are:

1. The low fidelity models investigated do not sufficiently capture aerodynamic

interactions between the coaxial rotors.

2. The propeller had a negligible effect on the acoustics of the coaxial rotor system. The difference in coaxial rotor noise between the full helicopter and airframe configurations was less than 1 dB.

3. The airframe had a negligible effect on the acoustics of the upper coaxial rotor ($\sim$ 2 dB) but caused an increase of approximately 6 dB (10 dBA) for the lower rotor. This would indicate the upwash from the fuselage and proximity of the tail cause a non-negligible increase in noise.

4. The airframe had a significant impact on the propeller acoustics. The observers far upstream and downstream (ψ=180 deg and ψ=0 deg) saw an increase of 40dB while those underneath the helicopter saw a decrease of 10 dB. However, the propeller noise is still a magnitude (10 dB) below the main rotor in this configuration.

5. The full helicopter had a slight impact on the propeller acoustics. Some observers at similar elevations with the helicopter (θ <=10 deg) would experience a 3 dB increase. Most observers underneath the helicopter would experience a 3 dB decrease or no noticeable change. Overall, the impact is negligible compared to the airframe impact on the propeller.

6. The airframe has a small impact on the total noise of approximately 6 dB (10 dBA). Based on the location (ψ=0 deg, θ <10 deg) and A-weighting, the propeller is the primary contributor to this increase. This causes a greater

number of observers to experience 120 dB noise.

7. The total rotor noise in dB is dominated by the coaxial rotor system. The coaxial rotors are approximately 5-10 dB louder than the propeller at all observer locations. The majority of observers hear the coaxial rotors twice as loud as the propeller. This was observed in all configurations.

8. The total rotor noise in dBA is dominated by the propeller. The propeller's primary frequencies (250 and 500 Hz) are 10x higher than the coaxial rotor system. This results in a -40 dB weighting for the coaxial rotors and less than -10 dB weighting for the propeller. This results in a maximum noise for some observers of 110 dBA.

6.4 Future Work

The predicted noise examined in this thesis is greater in magnitude than typically expected for helicopters. This is likely caused by the proximity of the analyzed observer hemisphere to the rotor disks compared to other studies ($\sim$ 80 ft). Previous studies, such as Sharma et al. ([14]), have predicted similar magnitudes of noise for a coaxial rotor system in isolation. However, it is uncertain whether the magnitude of the sound pressure level observed in this thesis is realistic. Therefore, it is necessary to conduct wind tunnel or flight tests to validate and verify the acoustic data in this thesis.

While this thesis provides a framework for the analysis of the interactional effects on acoustic prediction for a coaxial compound helicopter, the observed trends

might only apply for this flight condition. The 150-knot forward flight speed is a moderate speed that still has a relatively high main rotor RPM and low propeller thrust. This framework should be used to analyze different forward flight speeds to observe the effect on the trends observed in this thesis. It would be useful to quantify at which flight speed if any, the propeller begins to dominate the total rotor noise. Furthermore, the coaxial rotors' RPM changes based on forward flight speed as well. This would not only alter the blade loading and airloads but also how and where the rotor wakes interact with the fuselage and propeller. Therefore, it is recommended to expand this framework to different forward flight speeds to provide a greater understanding of the airframe and coaxial rotor effects on the propeller.

Along these same lines, the airframe was analyzed in the CFD but was not directly analyzed in the acoustic code, ACUM. The presence of the airframe would affect the propagation of noise from both coaxial rotors as well as the propeller. This could change the amount of noise observers hear as well as the shape of the observer contours. The pressure fluctuations on the fuselage itself would also change per configuration and flight speed as the rotor wake propagation changes. It is recommended to dive deeper into the acoustics code to enable the analysis of stationary objects and their effect on the noise.

Furthermore, this thesis calculates the compact chord airloads from the CFD surface pressure as the input into the acoustics code. The compact chord assumption is a simplification that somewhat reduces the fidelity of the acoustic analysis. It is recommended to expand ACUM to use the complete surface pressure data directly from CFD. This would not only increase the accuracy of the rotating blade solutions

but could also simplify the addition of stationary objects within the acoustics code.

This thesis proves that simulating multiple aerodynamic bodies and capturing the accompanying aerodynamic interactions will affect the acoustic prediction of the vehicle. This becomes increasingly important as the FVL community turns towards more advanced compound configurations. There is more research to be done not only for the compound coaxial configuration but for other novel compound configurations. This thesis provides a good framework for future investigations on the impact of aerodynamic interactions on acoustics.

Bibliography

[1] Mike Hirschberg. Jmr technology demonstration update: The road to future vertical lift. *Vertiflite*, 62, No. 7:22–27, 2016.

[2] A.J. Ruddell. Advancing blade concept (abc^{TM}) development. *Journal of the American Helicopter Society*, 22, No. 1:13–23, 1977.

[3] Ashish Bagai. Aerodynamic design of the sikorsky x2 technology demonstrator^{TM} main rotor blade. *64th Annual Forum of the American Helicopter Society*, 64:29, 2008.

[4] Jack E. Marte and Donald W. Kurtz. A review of aerodynamic noise from propellers, rotors, and lift fans. Technical report, January 1970.

[5] A.S. Morgans, S.A. Karabasov, A.P. Dowling, and T.P. Haynes. Transonic helicopter noise. *AIAA Journal*, 43, No. 7:1512–1524, 2005.

[6] Harvey H. Hubbard. *Aeroacoustics of Flight Vehicles: Theory and Practice*, volume 1. 1991.

[7] Centers for Disease Control and Prevention. What noises cause hearing loss? Available at `https://www.cdc.gov/nceh/hearing_loss/what_noises_cause_hearing_loss.html` (2019/10/7).

[8] Vera Klimchenko, Ananth Sridharan, and James Baeder. Cfd/csd study of the aerodynamic interactions of a coaxial rotor in high-speed forward flight. 2017.

[9] Vera Klimchenko and James Baeder. Cfd/csd study of interactional aerodynamics of a coaxial compound helicopter in high-speed forward flight. January 2020.

[10] Puneet Singh and Peretz Friedmann. A computational fluid dynamics based viscous vortex particle method for coaxial rotor interaction calculations. 05 2017.

[11] Douglas Boyd, Casey Burney, and David A. Conner. Acoustic predictions of manned and unmanned rotorcraft using the comprehensive analytical rotorcraft model for acoustics (carma) code system. January 2005.

[12] Hyo Kim, Karthik Duraisamy, and Richard Brown. Effect of rotor stiffness and lift offset on the aeroacoustics of a coaxial rotor in level flight. 1, 01 2009.

[13] Zhongqi Jia, Seongkyu Lee, Kalki Sharma, and Kenneth Brentner. Aeroacoustic analysis of a lift-offset coaxial rotor using high-fidelity cfd/csd loose coupling simulation. *Journal of the American Helicopter Society*, 01 2019.

[14] Kalki Sharma, Kenneth S. Brentner, Zhongqi Jia, and Seongkyu Lee. Aeroacoustic predictions of the free-wake model, vortex particle method, and computational fluid dynamics for a coaxial rotor system. January 2020.

[15] Wayne Johnson. *Lift-Offset Compound Design Background, X2TD, JMR ME1A Status and Plans*. Ames Research Center, Moffett Field, California, 2011.

[16] M. J. Bhagwat and J. G. Leishman. Time-accurate modeling of rotor wakes using a free-vortex wake method. *Journal of Aircraft*, 39, No. 5:759–775, September-October 2002.

[17] P. Anusonti-Inthra. The effects of the fuselage on a coaxial rotorcraft performance, aerodynamics, and structural dynamics. *American Institute of Aeronautics and Astronautics*, pages 1–15, 2019.

[18] B. Min, B. Moffitt, P.O. Bowles, B.E. Wake, and P.F. Lorber. Analysis and experimental testing of s-97 raider propeller. *AHS International*, 2018.